Icarus 213 (2011) 636–654

Contents lists available at ScienceDirect

Icarus

journal homepage: www.elsevier.com/locate/icarus

Stratospheric superrotation in the TitanWRF model

Claire E. Newman [a,*], Christopher Lee [a], Yuan Lian [a], Mark I. Richardson [a], Anthony D. Toigo [b]

[a] Ashima Research, Suite 104, 600 South Lake Avenue, Pasadena, CA 91106, USA
[b] The Johns Hopkins University, Applied Physics Laboratory, 11100 Johns Hopkins Road, Laurel, MD 20723, USA

ARTICLE INFO

Article history:
Received 2 December 2010
Revised 25 March 2011
Accepted 25 March 2011
Available online 5 April 2011

Keywords:
Titan
Atmospheres, Dynamics

ABSTRACT

TitanWRF general circulation model simulations performed without sub-grid-scale horizontal diffusion of momentum produce roughly the observed amount of superrotation in Titan's stratosphere. We compare these results to Cassini–Huygens measurements of Titan's winds and temperatures, and predict temperature and winds at future seasons. We use angular momentum and transformed Eulerian mean diagnostics to show that equatorial superrotation is generated during episodic angular momentum 'transfer events' during model spin-up, and maintained by similar (yet shorter) events once the model has reached steady state. We then use wave and barotropic instability analysis to suggest that these transfer events are produced by barotropic waves, generated at low latitudes then propagating poleward through a critical layer, thus accelerating low latitudes while decelerating the mid-to-high latitude jet in the late fall through early spring hemisphere. Finally, we identify the dominant waves responsible for the transfers of angular momentum close to northern winter solstice during spin-up and at steady state. Problems with our simulations include peak latitudinal temperature gradients and zonal winds occurring ~60 km lower than observed by Cassini CIRS, and no reduction in zonal wind speed around 80 km, as was observed by Huygens. While the latter may have been due to transient effects (e.g. gravity waves), the former suggests that our low (~420 km) model top is adversely affecting the circulation near the jet peak, and/or that we require active haze transport in order to correctly model heating rates and thus the circulation. Future work will include running the model with a higher top, and including advection of a haze particle size distribution.

1. Introduction

A major feature of Titan's stratosphere is the presence of strong superrotation (the atmosphere rotating many times faster than the surface) at both equatorial and higher latitudes. This has been inferred from Voyager IRIS (e.g. Flasar et al., 1981, 2005) and Cassini CIRS (e.g. Achterberg et al., 2008a, 2011) temperature observations, and from stellar occultation measurements (e.g. Hubbard et al., 1993), as well as being measured directly from Earth using the Doppler shift of spectroscopic lines (e.g. Kostiuk et al., 2001) and the Doppler shift of the Huygens probe's radio signal (e.g. Folkner et al., 2006). The presence of a westerly zonal jet in the winter hemisphere is expected in an atmosphere with a single solsticial Hadley cell (which can stretch almost from pole to pole due to Titan's slow rotation rate) as this mean meridional circulation transports angular momentum at upper levels into the winter hemisphere. However, the presence of strong superrotation at the equator requires a different explanation. Hide's theorem (Hide, 1969; Schneider, 1977) demonstrates that a steady axisymmetric circulation in which angular momentum is dispersed diffusively (however weak the diffusion) cannot have an extremum of absolute angular momentum away from the boundaries, which in turn means that zonal winds cannot exceed those implied by an angular-momentum-conserving circulation. For the equator, this tells us that westerly winds can only be produced if diffusion of angular momentum is balanced by something other than the angular-momentum-conserving axisymmetric circulation, i.e., can only be produced by upgradient eddy fluxes of angular momentum. Thus equatorial stratospheric superrotation seems to require that angular momentum be transported either vertically from lower levels or horizontally toward the equator by some type of eddies. Gierasch (1975) and Rossow and Williams (1979) suggested a plausible mechanism by which this might occur, with angular momentum gained from the low latitude surface, transferred into the stratosphere and redistributed to higher latitudes by the mean meridional circulation, then returned to low latitudes at upper levels by poleward-propagating eddies produced in barotropically-unstable regions at the (low latitude) edge of the zonal jets.

Attempts to realistically simulate this aspect of Titan's stratosphere in atmospheric general circulation models (GCMs) have met with mixed success. (Note that Titan's equatorial troposphere is also superrotating, but is not a focus of the present study.) The first 3D Titan GCM, that of the Laboratoire de Météorologie

* Corresponding author.
E-mail addresses: claire@ashimaresearch.com (C.E. Newman), lee@ashimaresearch.com (C. Lee), lian@ashimaresearch.com (Y. Lian), mir@ashimaresearch.com (M.I. Richardson), toigo@astro.cornell.edu (A.D. Toigo).

0019-1035/$ - see front matter © 2011 Elsevier Inc. All rights reserved.
doi:10.1016/j.icarus.2011.03.025

Dynamique (LMD), produced significant equatorial superrotation (Hourdin et al., 1995). Their model atmosphere was overall very similar to that observed by Voyager and more recently by Cassini with respectively the IRIS and CIRS instruments (Flasar et al., 1981, 2005; Achterberg et al., 2008a, 2011). Unfortunately, the model that produced this result is no longer in use, and no in-depth analysis was ever published showing the mechanisms responsible for the strong equatorial superrotation. The LMD group currently runs a 2D (latitude-height) model. This model produces realistic amounts of superrotation by parameterizing the effects of eddies based on results from their 3D GCM (e.g., Luz et al., 2003; Rannou et al., 2004). The many results from their 2D model and their impressive match to observations are not discussed further here, however, as we are concerned primarily with the production of superrotation in 3D models by the eddies themselves, which 2D models inherently cannot address.

The inability of any group to reproduce the Hourdin et al. (1995) result became a common theme within the modeling community. The Köln (Cologne) Titan model (Tokano et al., 1999) suffers from weak superrotation (peak zonal winds of under 60 m/s, rather than the observed ~200 m/s), as does the TitanWRF v1 model (see Section 3.1.1) published in Richardson et al. (2007) and the Titan CAM (Community Atmosphere Model) of Friedson et al. (2009). Another model (Mingalev et al., 2006) achieves superrotation, but only by fixing atmospheric temperatures, whereas in reality the circulation produced would act to swiftly disrupt their imposed temperature structure, making this model internally inconsistent and thus unsatisfactory. Other published Titan models, while insightful for tropospheric methane studies, are confined to the troposphere only and use highly simplified radiative transfer schemes (e.g. Mitchell et al., 2006; Mitchell, 2008). While various reasons for failure had been suggested there remained a bias among modelers that the issue was fundamentally dynamical or numerical in nature (e.g. Friedson et al., 2009).

This proved to be correct, in the TitanWRF model at least. As described in Section 3.1.2, the most recent version of TitanWRF now successfully simulates the observed magnitude of superrotation, with the amount of imposed horizontal diffusion found to be the critical factor involved in obtaining this result. Section 3.2 compares TitanWRF results with available observations, while Section 3.3 describes the impact of resolution on results, and Section 3.4 shows TitanWRF predictions of the atmospheric circulation in different seasons. Section 4 then provides details of the mechanisms that both generate and maintain TitanWRF's equatorial superrotation. In Section 5 we summarize our findings and discuss future work.

2. PlanetWRF and the TitanWRF GCM

2.1. Overview

PlanetWRF is a multi-scale, planetary atmospheric model, developed from the terrestrial, limited-area WRF (Weather, Research and Forecasting) model as described in Richardson et al. (2007). The project began with the production of a global WRF model (see Section 2.2), followed by the generalization of parameters and addition of planetary physics to produce PlanetWRF and specifically the TitanWRF model (see Section 2.3). Although all results shown here use TitanWRF as purely a global model (or GCM), TitanWRF may also be run as a limited-area model, or as a multi-scale model with a global mother domain and embedded high-resolution 'nests.'

2.2. The global WRF model

When we began this project, the WRF model (v2.1.2 at that time) could be run with several nests embedded within the mother domain, but could not be run with a global mother domain due to the assumption of conformal grids. In a conformal grid, the mapping from real world to model spacing at each gridpoint is the same in the x and y directions, which prevents it from extending all the way to the poles. Major modifications to produce a global model thus included modifying the dynamical core to run with non-conformal grids (e.g. a simple cylindrical projection, lat–lon grid) and adding special treatment of polar boundary conditions and polar filtering of high latitude regions to prevent instabilities. Our original Titan GCM (TitanWRF v1, see Section 2.3) was based upon this version of global WRF.

Our modifications to the WRF model were then passed back to the WRF developers at the National Center for Atmospheric Research (NCAR), who over a period of time validated and improved on them, and they were subsequently included into a later WRF release (v3.0.1.1) so that the entire WRF community could benefit. This version of WRF also contained numerous other improvements and additions, as do all new releases.

Significantly, the NCAR team had identified some errors in our choice of map scale factors, predominantly relating to terms in the geopotential equation and the calculation of meridional wind tendencies. Although representing a tiny fraction of the total changes made, these errors were sufficient to produce overly-strong wind and temperature gradients at high latitudes when the model spun up vigorously (see Section 3.1.1). TitanWRF v2 is therefore based on this improved version of global WRF produced by NCAR, and provides us with greatly improved results, as described in Section 3.1.2.

2.3. The planetary WRF model

Once we had a global WRF base model, major modifications to produce a planetary version (PlanetWRF) included removing hard-wired 'Earth' settings from parameterizations of physical processes (e.g., boundary layer mixing schemes) and adding planet-specific treatments of radiative transfer for Mars, Titan and Venus. Early results were shown in Richardson et al. (2007). The Titan version of PlanetWRF, TitanWRF, uses a two-stream radiative transfer model to generate heating rates. Gas and haze optical properties are found using a modified version of the scheme described by McKay et al. (1989, personal communication 2004–2006). TitanWRF also uses a multi-layer subsurface heat diffusion solver, surface energy balance solver, a non-local boundary layer diffusion solver, and horizontal subgrid-scale diffusion that can be prescribed (fixed) or calculated from the resolved-wind deformation, though as discussed in Section 3.1 we find optimum results when no horizontal diffusion is used. The model incorporates the impact of Saturn's gravitational field as Titan moves around Saturn in an eccentric orbit (e.g. Tokano and Neubauer, 2002) by including tidal accelerations into the momentum equations. The model used in this work includes no spatial variations in topography, albedo, or thermal inertia.

For this work, TitanWRF was run as a global, latitude–longitude, hydrostatic model with 54 σ' (modified-sigma) layers in the vertical from the surface to ~420 km, where $\sigma' = (P - P_{top})/(P_{surf} - P_{top})$, with P = pressure. The standard horizontal resolution used was 5.625° in longitude and 5° in latitude, though results are also shown using half this resolution in Section 3.3. At the standard model resolution, one Titan year runs in ~3.5 actual days using 24 processors on the Pleiades cluster at the NASA Ames High End Computing center.

We typically begin new TitanWRF simulations with the atmosphere at rest with respect to the surface of Titan, and with either a globally-uniform temperature profile (based on the observed global-mean profile) or an isothermal atmosphere, the latter becoming very similar to the former in only tens of Titan days of

radiative forcing. The model is then run until the atmosphere is fully spun up, i.e., has reached a point at which the seasonal cycle approximately repeats from year to year. Exceptions are 'restart' simulations begun from the spun-up state of a previous run.

For the remainder of this paper, 'year,' 'day' and 'hour' will refer to a Titan year, day and hour, as these have a direct relationship to the timescales of the applied solar forcing on Titan whereas Earth years, days and hours clearly do not. All units, such as ms^{-1}, will continue to be in SI, however.

3. Stratospheric superrotation in TitanWRF

3.1. The importance of low horizontal diffusion in producing significant superrotation

3.1.1. Results using TitanWRF v1

We ran the TitanWRF v1 GCM for several years until the atmosphere reached a steady, 'spun up' state. However, as described in Richardson et al. (2007), we originally produced about an order of magnitude less superrotation than observed. Fig. 1 shows zonal-mean temperatures, and Fig. 2 zonal-mean zonal winds, for the period $Ls \sim 293°–323°$ as observed by Cassini CIRS (top left plots) and produced by three TitanWRF simulations. Our original TitanWRF v1 results are shown at the top right of Figs. 1 and 2, and reveal an atmosphere with very weak latitudinal temperature gradients and a weak winter hemisphere zonal jet peaking at under 30 m/s.

We investigated possible reasons for this weaker-than-observed superrotation, and were finally able to attribute it to the amount of imposed (parameterized) horizontal diffusion inside TitanWRF. Typically, GCMs are run with imposed horizontal diffusion used to parameterize the effects of sub-grid scale eddy-mixing of heat and momentum, though in practice these schemes also act to prevent the growth of numerical instabilities. We experimented with different forms and magnitudes of diffusion (e.g., constant coefficient; Smagorinsky; hyper-diffusion), but ultimately found that only by setting the imposed horizontal diffusion to effectively zero could we obtain a winter hemisphere zonal jet with approximately the observed location and magnitude.

This result suggests that the processes responsible for superrotation in Titan's atmosphere are exceptionally sensitive, and are adversely impacted by any horizontal smoothing of temperature and wind gradients that result from a diffusion scheme, far more so than we see in Earth or Mars GCMs. This is most likely because the radiative forcing on Titan is far weaker than on Earth or Mars, thus any gradients produced are more easily destroyed.

The zonal-mean temperatures and zonal winds obtained after nearly 5 years of using zero horizontal diffusion in TitanWRF v1 are shown in the bottom left of Figs. 1 and 2, respectively. They show many similarities to the CIRS results shown in the top left plots. As already visible in these TitanWRF v1 results, however, as jet speeds increased so too did unrealistically sharp gradients near the poles, and the model became unstable soon after this point (Newman et al., 2008). These deficiencies had not shown up in our weakly superrotating Titan simulations or in simulations using the strongly radiative-forced MarsWRF model.

3.1.2. Results using TitanWRF v2

During this period, the WRF development team at NCAR had incorporated our global WRF modifications into an upcoming WRF release (which included numerous other desirable features, such as greater parallelizability and thus shorter run times). In doing so, they had identified and corrected a small number of errors in the map scale factors we introduced during our globalization of the dynamical core (see Section 2.2). We thus integrated our planetary modifications into this WRF release to produce TitanWRF v2, and again attempted to run the model with zero horizontal diffusion until it reached a steady state.

TitanWRF v2 proved to be far more stable than TitanWRF v1 as the high-latitude zonal jets develop: the model now spins up to steady state without instabilities developing, with no sharp gradients occurring near the poles, as shown in the bottom right plot of

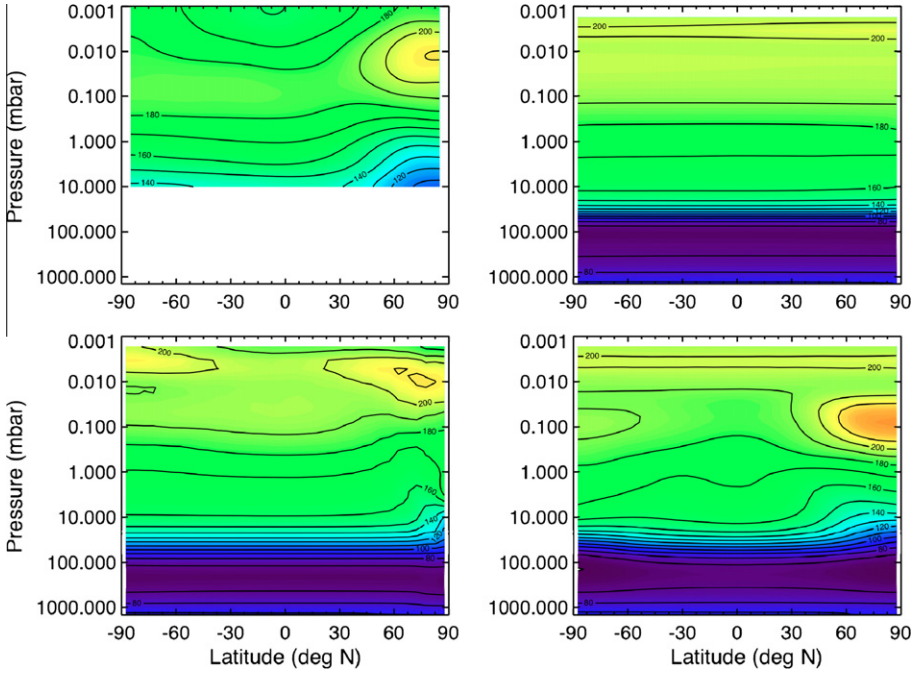

Fig. 1. Zonal-mean temperatures (K) for $Ls \sim 293°–323°$, retrieved from Cassini CIRS data (top left, provided by the Cassini dynamics team using the techniques of Achterberg et al. (2008a)), and as modeled by a steady state year (year 12) of a TitanWRF v1 simulation with standard diffusion (top right), the final year (year 4) of a TitanWRF v1 simulation with zero horizontal diffusion (bottom left), and a steady state year (year 75) of a TitanWRF v2 simulation with zero horizontal diffusion (bottom right). The TitanWRF v1 simulation with zero horizontal diffusion became unstable and crashed during year 5.

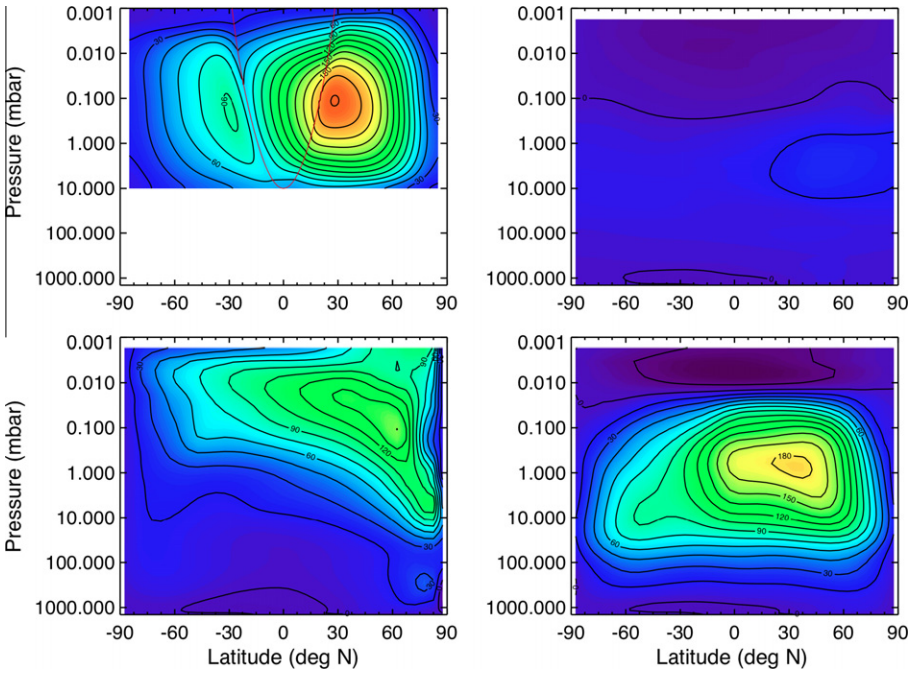

Fig. 2. As in Fig. 1, but showing zonal-mean zonal winds (m/s). The top left plot shows winds inferred from CIRS temperatures as in Flasar et al. (2005). The red line shows the latitudinal limit of the gradient wind balance assumption, and winds are linearly interpolated across this region.

Fig. 2. A side-effect is a significant increase in the time required to spin-up the model from rest, 75 years, suggesting that the previous errors were significantly impacting our zero diffusion results. (Note that we also performed TitanWRF v2 simulations using increased horizontal diffusion, and verified that weak superrotation is still produced, with results very similar to those produced using TitanWRF v1 with the same diffusion scheme and coefficients.)

Figs. 3 and 4 show the 'superrotation index' (the total angular momentum of an atmospheric layer divided by the total angular momentum of that layer at rest) for respectively years 1–15.5 and years 45–74 of a TitanWRF v2 simulation with zero imposed horizontal diffusion. Note that plotting superrotation index gives undue weight to low-density regions, compared with plotting angular momentum itself (as in Fig. 11), thus emphasizing regions with the largest zonal wind speeds rather than those with the largest angular momentum. During the initial years of the simulation there are long periods of rapid spin-up at pressures below 20 mbar, i.e., net gains in atmospheric angular momentum at the expense of the angular momentum of the solid surface (see Section 3.1). By the final years of the simulation, however, the spin-up is very gradual, with net gains from year to year finally ceasing when the model reaches steady state at about 69 years in.

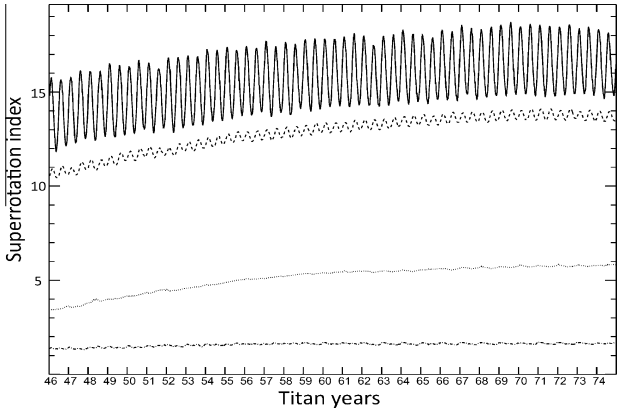

Fig. 4. As in Fig. 3, but showing years 45–74 only. The simulation reaches steady state after roughly 69 years.

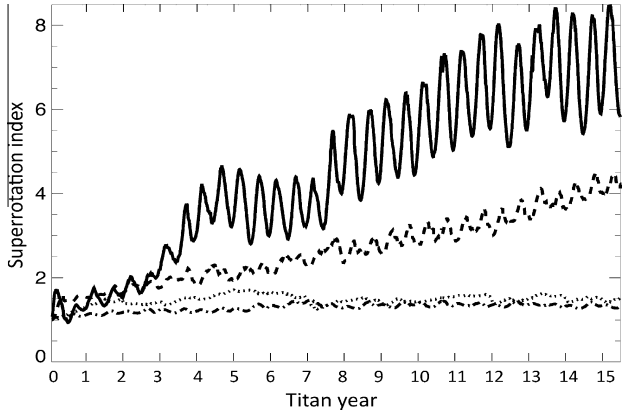

Fig. 3. Superrotation indices in four broad layers for the first 15.5 years of a standard horizontal resolution (5.625° × 5°) simulation with zero horizontal diffusion and no top level damping. Layers are: 0.0087–2 mbar (solid), 2–20 mbar (dashed), 20–200 mbar (dotted) and 200 mbar-surface (dot-dashed).

Superimposed on the overall pattern of spin-up is a bi-annual oscillation, as seen more clearly in Fig. 5 showing results for a steady state year. In the uppermost 2 mbar of TitanWRF's stratosphere, superrotation peaks at ∼30° of *Ls* after equinox, and minima occur ∼30° after solstice; lower in the stratosphere, these timings are shifted ∼30° later. This pattern is a result of the seasonal variation in the mean meridional circulation, as shown in the mass streamfunction plots at the bottom of Figs. 8 and 9, which affects angular momentum transfers within the atmosphere. Around equinox, upwelling at low latitudes brings eastward angular momentum (gained from the low latitude surface, see Section 3.1) up into the upper stratosphere. Around solstice, upwelling (and the arrival of eastward angular momentum) occurs at high summer latitudes, but is more than compensated for by downwelling at the location of the strong westerly jet (see Fig. 8 zonal wind plots) in the winter

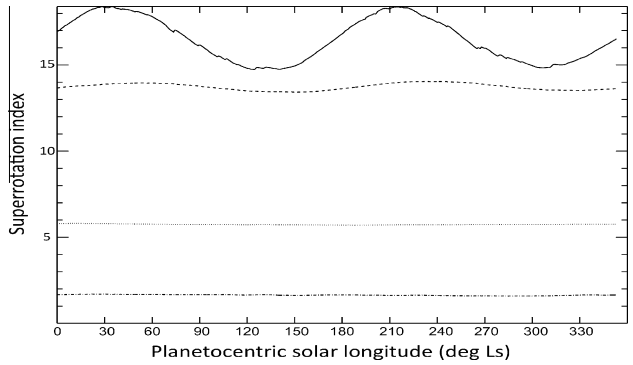

Fig. 5. As in Fig. 3, but showing year 75 only.

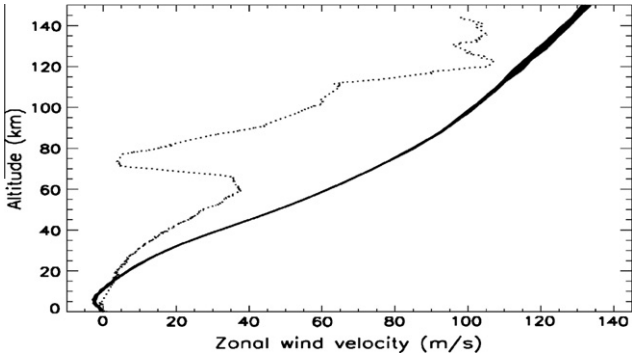

Fig. 6. TitanWRF v2 zonal wind profiles from the surface up to 150 km altitude for the location and date of Huygens's arrival (10°S, *Ls* = 300.5) for 64 different local times of day (solid lines) compared with Huygens Doppler wind measurements (dotted line) taken from the PDS (Folkner et al., 2006).

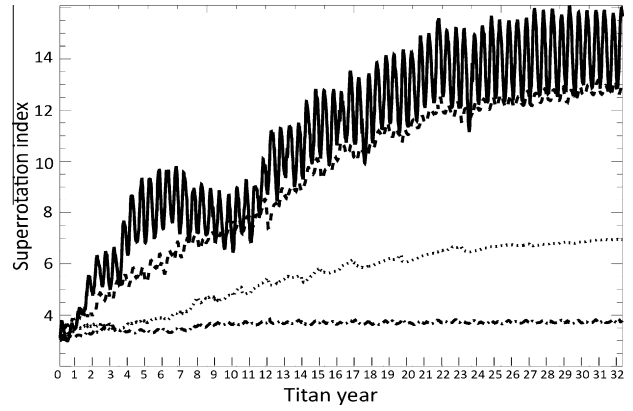

Fig. 7. As in Fig. 3, but for a simulation run at half the resolution (11.25° × 10°). Just over the first 28 Titan years are shown. The simulation reaches steady state after roughly 24 years.

hemisphere, which removes angular momentum from the upper stratosphere and returns it toward the surface. Hence there is a bi-annual peak in upper stratospheric angular momentum shortly after both equinoxes, with a minimum shortly after both solstices. Angular momentum exchange and transport are discussed in more detail in Section 3.1.

3.2. Comparison between TitanWRF v2 results and observations

The steady state TitanWRF v2 results for *Ls* ~ 293°–323° (bottom right of Figs. 1 and 2) reveal many similarities to the temperatures and zonal winds observed by Cassini CIRS (top left of Figs. 1 and 2) in this season. Note that the CIRS results are complicated by the need to define a lower boundary condition for their wind retrievals. They set the wind at 10 mbar to four times the solid body rotation rate, a rather large (albeit necessary) assumption, and though this was chosen to be consistent with Huygens it slightly underestimates the true wind speed there compared to Huygens measurements (Folkner et al., 2006). As in the CIRS observations, peak TitanWRF v2 temperatures of over 200 K occur high above the winter (north) pole, and a peak zonal wind jet with winds well over 175 m/s is located between ~75°N and 20°S, with peak equatorial zonal winds of over 150 m/s. However, there are several mismatches too, most obviously the difference in level between the observed and modeled temperature and wind maxima; observed temperatures [winds] peak at ~0.01 mbar [~0.1 mbar], while modeled temperatures [winds] peak at ~0.08 mbar [~0.8 mbar], approximately 60 km (about one scale height) lower. Another prominent difference is the simulated increase (rather than the observed decrease) in temperature above 0.01 mbar. All of the above may be a side-effect of the relatively low placement of the model top with respect to the interesting atmospheric features, or of the lack of active haze transport allowing radiative–microphysical–dynamical feedbacks within the model atmosphere. The northern high latitude heating (hence the associated wind jet) in this season occurs during polar night and is a dynamical phenomenon associated with adiabatic heating in the downward branch of the solsticial Hadley cell, thus problems with this circulation – due either to a low model top or to the lack of correct haze forcing in the 'driver' region – may have led to the mismatch described. Also, in reality the atmosphere of Titan is sufficiently extended that significant heating still occurs in the stratosphere at latitudes for which the surface is in polar night (e.g. Achterberg et al., 2008a); however, we do not currently include this effect in TitanWRF. These issues will be addressed in future work.

Cassini CIRS observations also revealed a small (~4°) displacement of the axis of symmetry of the zonal mean flow with respect to the pole over a range of pressures (Achterberg et al., 2008b). We find negligible displacement of the pole in TitanWRF at the pressures observed, and though we do produce a small but significant displacement of the axis of symmetry at higher altitudes it is unclear how or if this is related. However, given suggestions that the observed displacement may increase with altitude (Achterberg et al., 2008b) we may be partially capturing the effect, and this will be investigated in future work.

Fig. 6 shows TitanWRF v2 zonal wind profiles from the surface up to 150 km altitude for the location and date of Huygens's arrival for 64 different local times of day, as well as the Huygens Doppler wind measurements for comparison (Folkner et al., 2006). Well below the large dip in measured zonal wind speed (centered at ~80 km) we match observations reasonably well, with wind speeds of ~5 m/s at 20 km altitude, but by 60 km we predict wind speeds of ~60 m/s rather than the 40 m/s observed, and fail to predict any dip in wind speed between 60 and 120 km. Well above this dip, however, we again show a reasonable match to observations, predicting wind speeds of ~115 m/s (only ~10 m/s faster than observed) at 120 km.

Overall, high zonal winds appear to persist far lower in the model atmosphere than inferred by Cassini CIRS or measured directly by the Huygens probe, though it is possible that wave activity may have produced transient lower zonal winds (in particular the strong dip in wind speed centered at ~80 km) during the Huygens descent that are not representative of the background wind speed. Whether the wind speed dip is a persistent or transient feature, however, TitanWRF v2 does not reproduce it in simulations for which we produce the observed strong stratospheric superrotation, suggesting that we are either misrepresenting the distribution

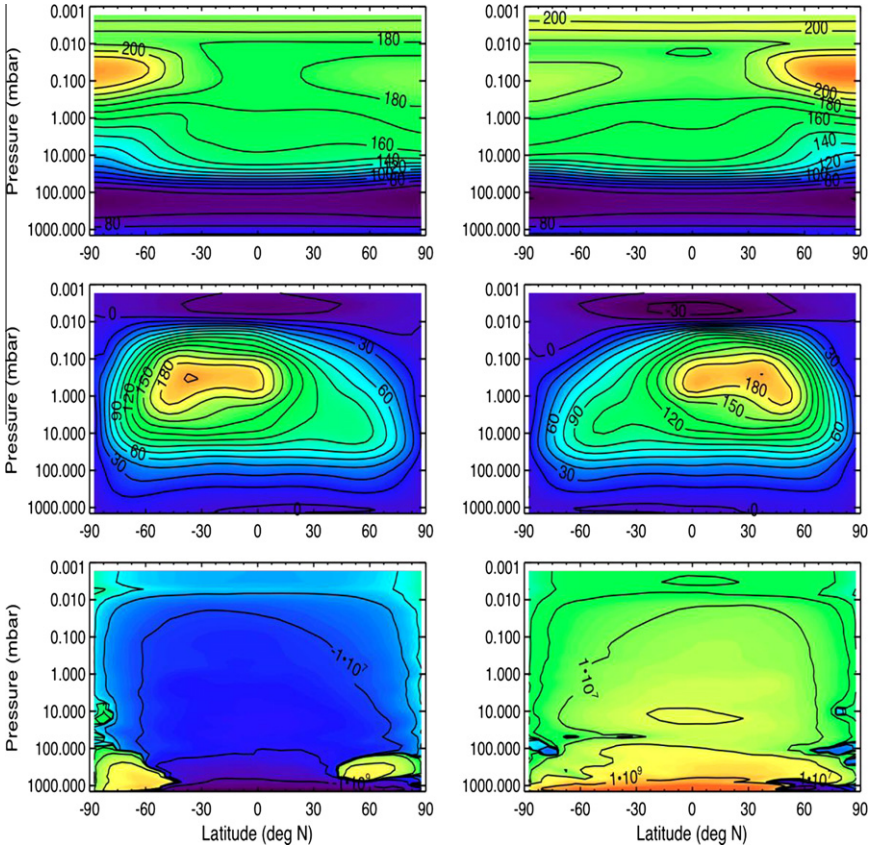

Fig. 8. Zonal-mean temperatures (in K, top row), zonal winds (in m/s, middle row) and mass streamfunction (in kg/s, bottom row) from a fully 'spun up' (steady state) year of the standard TitanWRF v2 simulation (year 75), averaged over 12 Titan days around northern summer ($Ls \sim 90°$, left column) and winter ($Ls \sim 270°$, right column) solstice. Positive streamfunction values indicate clockwise rotation.

of atmospheric heating or are missing some wave generation mechanism. Gravity waves, which grow with height and break aloft, redistributing momentum, are estimated to be significant in Titan's atmosphere (Strobel, 2006). However, TitanWRF v2 only includes the effects of vertically-propagating waves that are resolved at our standard resolution of ~5° and generated over a smooth surface; it does not currently include a parameterization of sub-grid-scale gravity waves or (in our standard model) any surface topography.

To summarize, it appears that explicit horizontal diffusion of heat and momentum, imposed within TitanWRF's dynamical core to represent sub-grid scale mixing, was originally too high and was effectively dissipating the waves postulated by Gierasch (1975) and Rossow and Williams (1979) to cause the equatorward angular momentum transport that accelerates the equatorial flow. Using zero horizontal diffusion, we now produce significant latitudinal temperature gradients and superrotation, albeit with zonal winds and temperatures that peak roughly one scale height lower than observed in the real atmosphere.

3.3. Impact of resolution on results

We also ran TitanWRF v2 with a horizontal resolution of $11.25° \times 10°$ (i.e., at half our standard resolution), and found the impact on our results to be significant. Fig. 7 shows the superrotation index for the first ~32 years of this low-resolution simulation. The model atmosphere now takes roughly 30 years to spin-up to a steady state, less than half the time required for our standard resolution simulation, however the peak superrotation index by this point is slightly smaller (~16 for the upper layer shown, rather than ~19). This suggests a dependence on horizontal resolution in terms of the generation and meridional propagation of waves required to drive superrotation in TitanWRF (see Section 4).

This result also motivates us to establish whether the peak superrotation achieved has converged by our standard resolution of $5.625° \times 5°$, or whether it would increase if resolution were increased further. We will investigate this in subsequent work. However, given the time requirements for our standard resolution simulation to reach steady state (~8 months of real time), we will most likely interpolate our steady state atmosphere from this simulation onto a higher-resolution ($2.8125° \times 2.5°$) grid, and proceed from there, rather than begin with the atmosphere at rest.

3.4. Seasonal variations

Figs. 8 and 9 show TitanWRF predicted zonal-mean temperatures, zonal winds and mass streamfunctions averaged over 12 days surrounding the four cardinal seasons. Fig. 8 shows both the northern summer ($Ls \sim 90°$, left) and winter ($Ls \sim 270°$, right) solstices, and demonstrates the high degree of symmetry between these seasons, with temperatures and winds at $Ls \sim 270°$ resembling the results already shown in Fig. 1 (which covers a slightly later time period). At solstice, the stratospheric circulation as shown by the mass streamfunction consists of a nearly pole-to-pole Hadley cell, with rising motion at high summer latitudes and descending motion above the winter pole. This descending motion produces strong adiabatic heating in the winter hemisphere, resulting in a temperature maximum high above the winter pole despite this portion of the model receiving no solar insolation at this time of year. The peak temperatures produced aloft in the

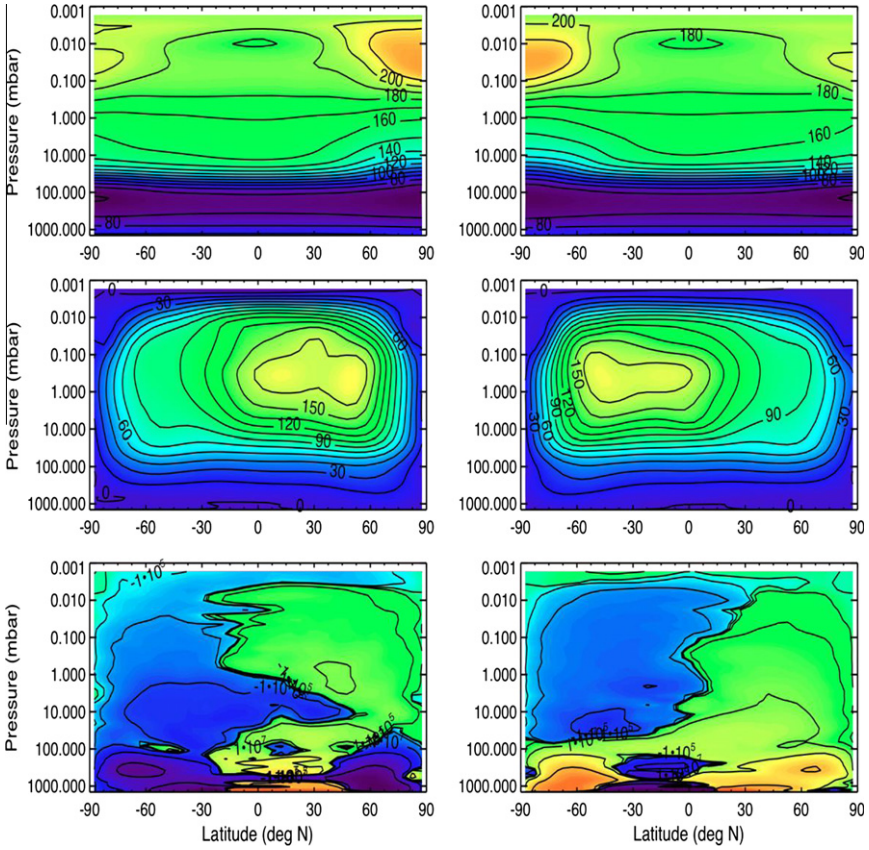

Fig. 9. As in Fig. 8 but for northern spring ($Ls = 0°$, left) and fall ($Ls = 180°$, right) equinoxes.

northern hemisphere during local winter (top right plot) are stronger than those produced during southern winter (top left plot), reflecting the stronger solar forcing during the former time period (which includes perihelion at $Ls \sim 278°$ (Hourdin et al., 1995)), which drives a stronger Hadley circulation (as shown by the streamfunction plots) and hence stronger downwelling and adiabatic heating. However, this slight asymmetry does not appear to significantly affect the overall latitudinal temperature gradient, or the zonal wind jets peaking at winter mid-latitudes that relate to the temperature gradient via the thermal wind equation. Small Ferrell cells also exist at high latitudes at northern summer, though are far weaker or absent in southern summer.

Fig. 9 shows both the northern spring ($Ls \sim 0°$, left) and fall ($Ls \sim 180°$, right) equinoxes. (Cassini arrived in orbit around Saturn after northern winter solstice at $Ls \sim 290°$, so by late 2010 had just covered the $Ls \sim 0°$ period shown.) At each equinox, two large Hadley cells dominate above ~30 mbar, with rising motion at low latitudes and descending motion over both poles. Below this, however, the circulation is more complex, with the streamfunction even reversing at some latitudes before transitioning to two smaller (less broad) Hadley cells that are less symmetric about the equator in the troposphere. The bulk of the temperature and wind field is again quite symmetric in latitude (i.e., about the equator) within each season, though remants of the preceding solstice's high-latitude winter hemisphere temperature gradients and enhanced zonal wind jets can be seen in their respective winter/spring hemispheres.

The circulation produced by TitanWRF has many similarities to that produced by Hourdin et al. (1995) using the only other three-dimensional GCM to have achieved significant stratospheric superrotation. In particular, the shape of the zonal wind jets during northern winter and spring is extremely similar over the pressure range shown (Hourdin et al.'s Fig. 8 is cut off at ~0.3 mbar), the main difference being the greater wind magnitudes in TitanWRF (a peak of ~180 m/s versus their ~120 m/s peak). The strong similarities, as well as the preliminary analysis of wave forcing that they present, suggests that similar processes to those identified in TitanWRF (see Section 4) may have been at work in their model as well. Interestingly, Hourdin et al. (1995) state that parameters in their horizontal dissipation scheme were chosen "somewhat arbitrarily," suggesting that they may also have used quite low amounts of horizontal diffusion without fully realizing the significance of this.

4. The mechanisms behind TitanWRF's equatorial superrotation

4.1. Equatorward angular momentum transfer in the steady state and transient model atmosphere

A major question for atmospheres with superrotating flow at the equator is how angular momentum builds up at low latitudes, as described above. Having achieved our goal of simulating a realistically superrotating stratosphere, we can now analyze the model atmosphere to deduce the probable cause. Any analysis of Titan's atmosphere is complicated by Titan's axial tilt (obliquity) which results in the seasonal variations in circulation shown in Figs. 8 and 9. Unlike Venus, which has zero obliquity, the 'steady state' (spun up) atmosphere is not approximately constant with time, but rather varies from season to season in an approximately repeating fashion from year to year. Our initial analysis showed a complex pattern of angular momentum variations, leading us to use a 'box model' approach, that of splitting the atmosphere into six regions and considering angular momentum changes and transports within and between them. The six regions were produced by

splitting the model domain vertically into two regions, and latitudinally into three, as shown in Fig. 10. In the vertical we define the 'lower atmosphere' as the region between the surface and slightly above the tropopause at ~110 mbar, and the 'upper atmosphere' as between this location and the penultimate model layer (at ~0.005 mbar). In the horizontal we define a southern region southward of 22.5°S; an equatorial region as between 22.5°S and 22.5°N; and a northern region as northward of 22.5°N.

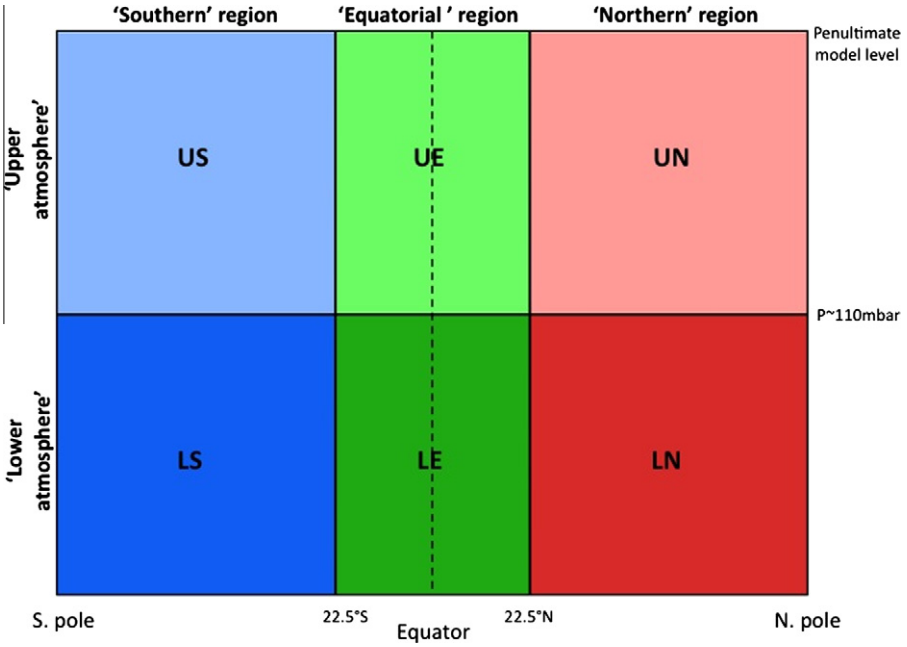

Fig. 10. Schematic showing the 'box model' used to analyse the regional dependence of angular momentum variations in TitanWRF output.

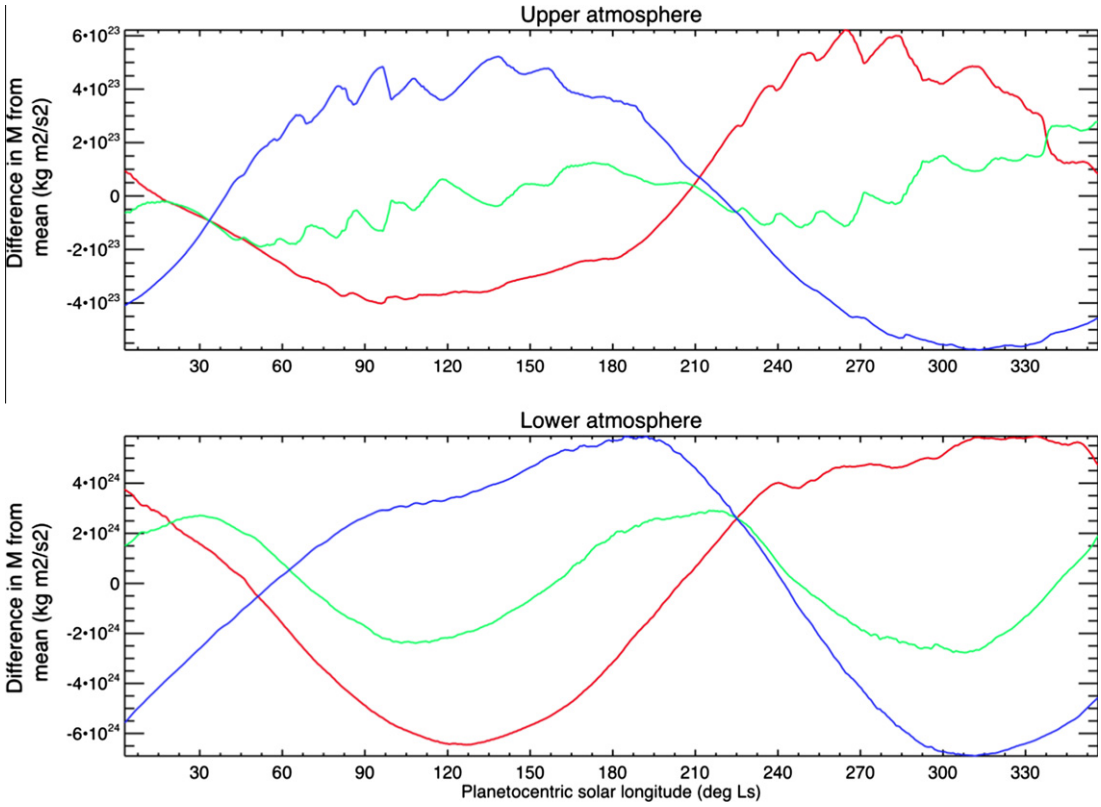

Fig. 11. Total angular momentum, M in kg m^2 s^{-1}, in the atmospheric regions defined in Fig. 10, for a spin-up year of the standard TitanWRF v2 simulation (year 12). The annual mean is subtracted so that all latitudinal regions can be clearly displayed on both plots (without the equatorial total angular momentum dominating). The upper plot shows results summed over the upper atmosphere region for the southern (US, in blue), equatorial (UE, in green) and northern (UN, in red) latitude regions. The lower plot shows results summed over the lower atmosphere region for the southern (LS, in blue), equatorial (LE, in green) and northern (LN, in red) latitude regions. Note that in the print version of this article, the lines colored red, green and blue are shown respectively as light gray, dark gray and black.

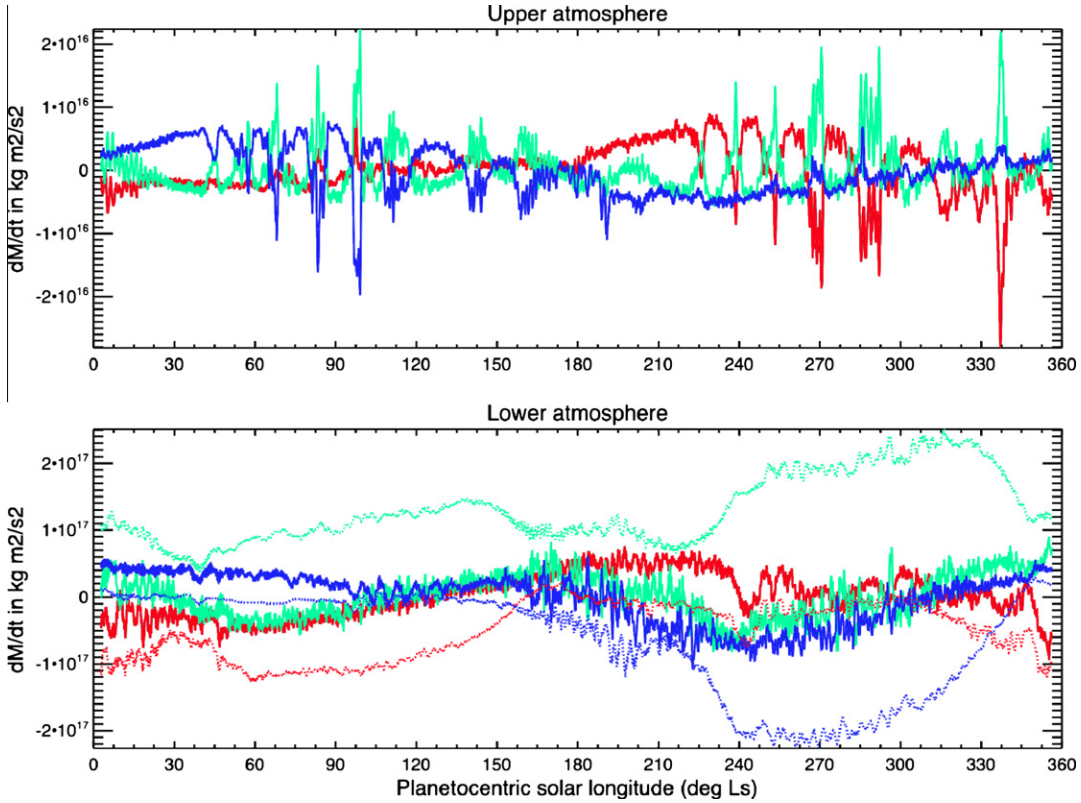

Fig. 12. As Fig. 11, but showing the rate of change of total angular momentum, dM/dt in kg m^2 s^{-2}, rather than M. Also shown in the bottom plot (as dotted lines) are the surface torques (in kg m^2 s^{-2}) exerted by the surface on the atmosphere, summed over the surface of each region.

In Fig. 11 we plot the total angular momentum, M, summed over each region, with the mean subtracted for clarity. In Figs. 12–14 we show the rate of change of total angular momentum, dM/dt, and the torque exerted by the surface on the atmosphere, T, again summed over each atmospheric region (though only surface winds, *etc.* are required to calculate T). In each figure the upper atmosphere region is shown at the top and the lower atmosphere region at the bottom, with the northern region in red[1], the southern region in blue, and the equatorial region in green. M and dM/dt are shown with solid lines, while T are shown with dotted lines.

The total angular momentum, M, in each model grid cell is given by

$$M = \Delta m \times [u + \Omega a \cos\phi] a \cos\phi = \frac{a^3 \Delta\phi \Delta\lambda}{g} [u + \Omega a \cos\phi] \cos^2\phi |\Delta P| \quad (1)$$

where Δm is the mass of the grid cell in kg, u is the zonal wind velocity in m/s, Ω is Titan's rotation rate in radians per second, a is Titan's radius in m, ϕ is latitude in radians, g is gravity in m/s^2, λ is latitude in radians, $\Delta\phi$ and $\Delta\lambda$ are the size of the grid cell in respectively latitude and longitude in radians, and ΔP is the pressure thickness of the grid cell in Pa.

The rate of change of total angular momentum, dM/dt, provides a sense of the 'acceleration' and 'deceleration' of each region, and dM/dt summed over the entire atmosphere should balance the net torque exerted on the atmosphere by the surface, which is determined by the pattern of surface zonal winds. The torque contribution from each surface grid cell, T, is given by

$$T = ta^2 \cos\phi_j \Delta\phi \Delta\lambda \quad (2)$$

where

$$t = -a \cos\phi \tau_e = -a \cos\phi \rho C_d (u^2 + v^2)^{1/2} u \quad (3)$$

and where τ_e is the surface zonal wind stress, u and v are respectively the zonal and meridional wind speed at the surface, and C_d is a drag coefficient depending on wind speed and stability parameters in the planetary boundary layer (see e.g. Ponte and Rosen, 1993). In practice, C_d was derived from TitanWRF's surface layer scheme (Hong and Pan, 1996).

4.1.1. Angular momentum transfer during the spin-up period

We are initially interested in how the fast equatorial superrotation was achieved in the TitanWRF v2 model, so we begin by looking at a year during rapid 'spin-up' of the model atmosphere, when the total angular momentum of the atmosphere is increasing significantly each year (as angular momentum picked up at the surface is distributed within the atmosphere). We choose year 12 of our standard TitanWRF v2 simulation, which took ~69 Titan years to spin-up completely (reach a steady state) as shown in Figs. 3 and 4.

4.1.1.1. The lower atmosphere. The bottom of Fig. 11 shows total angular momentum, M, for the lower atmosphere regions. The basic pattern for both the northern and southern regions is a gradual increase in M from mid-summer to ~spring equinox, followed by a rapid decrease during spring. This pattern is partly due to local gains from / losses to the surface, as seen in the torques, T, shown in Fig. 12 (dotted red and blue lines), which are in turn tied to the pattern of surface zonal wind (not shown). Easterly winds result in positive torques on the atmosphere, hence transfer of angular momentum from surface to atmosphere occurs where surface easterlies exist, and transfer from atmosphere to surface where there are surface westerlies, with the torque increasing as latitude

[1] For interpretation of color in Figs. 1, 2, 8–19, and 24, the reader is referred to the web version of this article.

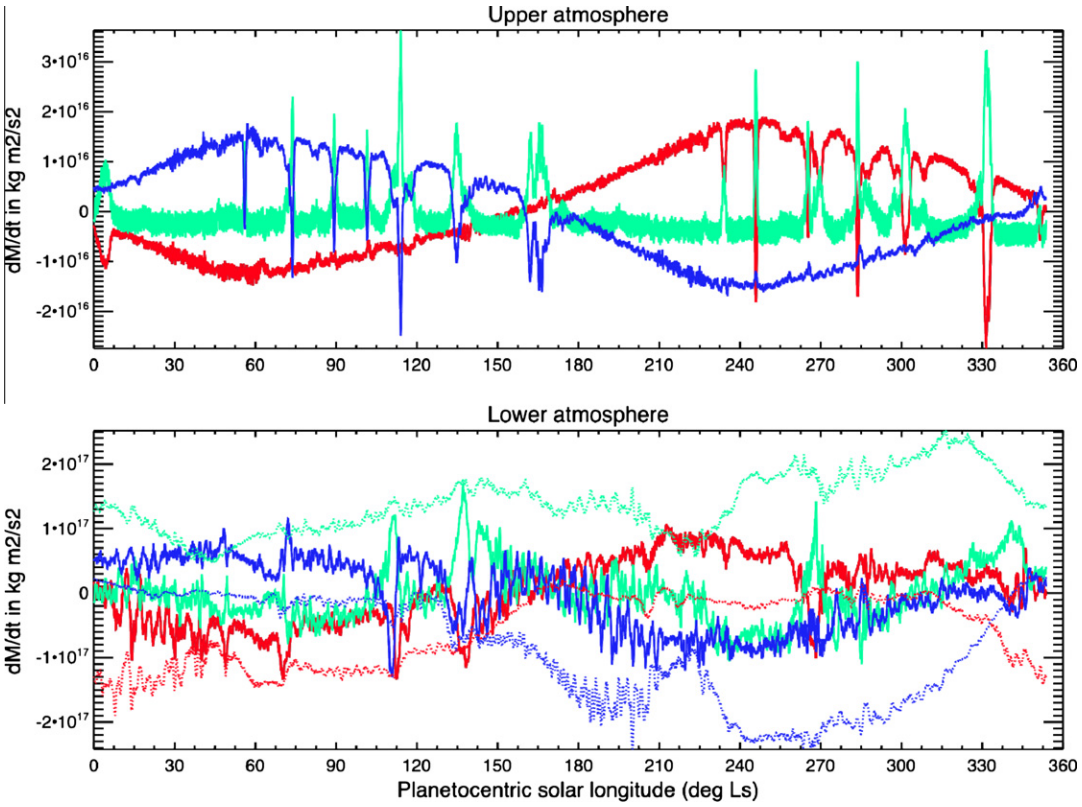

Fig. 13. As Fig. 12, but for a steady state year of the same simulation (year 75).

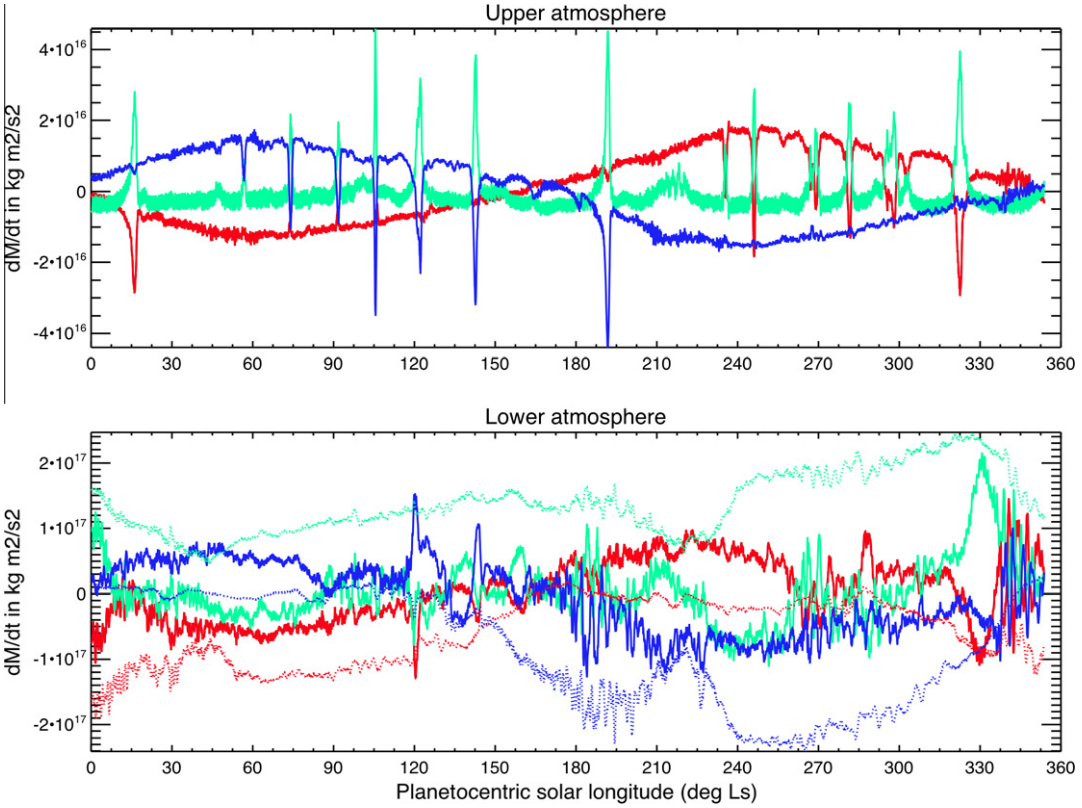

Fig. 14. As Fig. 12, but for a second steady state year of the same simulation (year 76) for comparison with Fig. 13 (showing year 75).

decreases for a given zonal wind speed (see Eqs. (2) and (3)). The northern and southern regions experience large negative torques, and thus lose significant angular momentum to the surface, in spring (when high-latitude surface westerlies peak) and summer (when strong westerlies occur at mid-latitudes, exerting more torque for a given wind speed), with very little net gain from the surface during the remainder of the year. However, the lower atmosphere in the northern and southern regions (red and blue solid lines, bottom of Fig. 11) also gains angular momentum from the equatorial lower atmosphere and from the stratosphere, producing an increase in M ($dM/dt > 0$ in Fig. 12) from late summer through to early spring. The greatest gains occur during fall as the solsticial Hadley cell develops, transporting more angular momentum into the fall hemisphere.

The equatorial lower atmosphere (green line, bottom of Fig. 11) shows a bi-annual oscillation in M, peaking ~30° after equinox with minima ~30° after solstice. However, this is roughly anti-correlated with the torque exerted on this region of the atmosphere by the equatorial surface (dotted green line, bottom of Fig. 12). In other words, rather than accelerating the equatorial atmosphere, angular momentum gained from the surface at low latitudes is rapidly transferred to higher latitudes in the fall/winter hemisphere or into the stratosphere. Surface easterlies thus continue to dominate over most of the equatorial region, hence the net torque on the atmosphere is always positive here. The torque peaks from late spring through late summer, when the solsticial Hadley cell drives strong cross-equatorial winds that are then turned westward on their approach to the equator by the Coriolis effect. Note that observations of dune morphologies on Titan have been used to suggest the presence of surface westerlies at low latitudes (e.g. Radebaugh et al., 2008), though we find no evidence in TitanWRF of dominant low latitude surface westerlies at any time of year.

4.1.1.2. The upper atmosphere. The upper atmosphere shows similar seasonal trends in M and dM/dt (top of Figs. 11 and 12 respectively), including the increase in angular momentum ($dM/dt > 0$) through most of the fall to late winter period in the northern and southern regions, producing peak M around or just after winter solstice as the single, solsticial Hadley cell carries angular momentum into the winter hemisphere. However, these seasonal trends are now interrupted by large perturbations in M, with increases in equatorial M coinciding with decreases in M in one – but not both – of the higher latitude regions (top of Fig. 11).

These perturbations are seen more clearly in dM/dt (top of Fig. 12), with large maxima in equatorial dM/dt coinciding very cleanly with large minima in either the northern or southern region. We will henceforth refer to them as 'transfer events,' as they clearly correspond to the transfer of angular momentum from one hemisphere toward the equator. Which type of transfer event occurs is completely controlled by the season, with equatorward transport of angular momentum always coming from the fall/winter hemisphere, i.e., from the south (blue troughs and green peaks) for $Ls \sim 30°$–$210°$, and from the north (red troughs and green peaks) for $Ls \sim 210°$–$30°$. These major events episodically increase the equatorial angular momentum in the upper atmosphere and, despite other periods during which dM/dt becomes slightly negative, there is a net increase in equatorial angular momentum over the course of the year shown.

This result shows that, at least in TitanWRF v2, the processes (presumably eddies) responsible for transporting angular momentum up-gradient back toward the equator – thus maintaining and growing the amount of equatorial superrotation – occur only sporadically, and over relatively short periods of time (tens of Titan days or less), rather than being a continual process lasting through a whole season or even the entire year.

4.1.2. Equatorial superrotation in the steady state atmosphere

Fig. 13 shows the same as in Fig. 12, but now for year 75 of this TitanWRF v2 simulation. By this time the model atmosphere has fully spun up (reached a steady state), thus we now focus on processes maintaining (rather than growing) the equatorial superrotation in the upper atmosphere. Note that, despite the variations shown, there is no net change in angular momentum of any region over the course of several Titan years once the model has reached steady state. There are some notable differences between the spin-up and steady state years, the first being the shorter duration of the transfer events (apart from those occurring shortly before equinox) in the upper atmosphere. It thus appears that, in its balanced state, the atmosphere experiences shorter periods of instability. Another notable difference is in the lower atmosphere, where in the spun-up year several large increases in angular momentum occur (at e.g. $Ls \sim 110°$, 140°, 265° and 340°), coinciding with angular momentum decreases in both the northern and southern regions. Unlike those in the upper atmosphere, these equatorial increases thus appear to be due to equatorward angular momentum transfers from *both* hemispheres, and will be investigated further in a subsequent paper devoted to the troposphere.

It is interesting to compare the timings of these transfer events in spin-up and steady state years (years 12 and 75, in Figs. 12 and 13, respectively) and also in two steady state years (years 75 and 76, shown in Figs. 13 and 14, respectively). Although the seasonal pattern remains the same in all years, with transfer events always occurring between early fall and early spring in first the southern then northern hemisphere, the events do not generally occur at the same Ls, as might be expected if they were directly tied to seasonal changes in the solar forcing. If, however, these events are eddies triggered by the gradual build-up of instabilities tied to a slowly-varying circulation that has intrinsic interannual variability, we would expect more variability in their timings, as demonstrated here. Interestingly, while years 75 and 76 differ considerably in the timings of their southerly (from the south) transfer events – in fact, year 76 is the only year shown with such an event well into spring – the timings of their northerly transfers are remarkably similar until almost spring. However, this is a fluke and does not occur in all years.

Now that we have identified when equatorward angular transfer occurs, the next step is to establish how (Section 4.2) and why (Section 4.3) and finally to identify what waves are primarily responsible (Section 4.4).

4.2. Wave-driven angular moment transport in the TitanWRF model

We can demonstrate that the modeled up-gradient angular momentum transport toward the equator is due to eddies by examining the model output using the Transformed Eulerian Mean (TEM) formulation of Andrews and McIntyre (1978). The zonal momentum equation can be rewritten using the TEM formulation to separate out the mean and eddy contribution, as given in e.g. Andrews et al. (1987). The equation becomes:

$$\underbrace{\frac{d\bar{u}}{dt}}_{term1} = \underbrace{-\overline{v^*}\left[\frac{1}{a\cos\phi}\frac{d\bar{u}\cos\phi}{d\phi} - f\right]}_{term2} - \underbrace{\overline{w^*}\frac{d\bar{u}}{dz}}_{term3} + \underbrace{\frac{1}{\rho_0 a\cos\phi}\nabla\underline{F}}_{term4} + \underbrace{\overline{X}}_{term5} \quad (4)$$

where a is Titan's radius, t is time, ϕ is latitude, u is zonal wind, an overbar indicates the zonal mean, f is the Coriolis parameter = $2\Omega \sin\phi$, where Ω = Titan's rotation rate in radians/s, z = log pressure coordinate = $\ln(P_0/P)$, where P_0 is a reference pressure of 1.44e5 Pa, X contains other processes (e.g., diffusion, damping), ρ_0 is reference density = $P/(R'T_0)$, where P = pressure, T_0 = a reference

pressure of 120 K and R' is the gas constant for Titan's atmosphere, and where $\underline{F}$ is the Eliassen-Palm flux vector (see below). The residual mean circulation components in the meridional and vertical directions are given by respectively

$$\overline{v^*} = \bar{v} - \frac{1}{\rho_0}\frac{d}{dz}\left[\frac{\rho_0 \overline{v'\theta'}}{d\bar{\theta}/dz}\right] \quad \text{and} \quad \overline{w^*} = \bar{w} + \frac{1}{a\cos\phi}\frac{d}{d\phi}\left[\frac{\cos\phi\,\overline{v'\theta'}}{d\bar{\theta}/dz}\right] \tag{5}$$

where $'$ indicates the perturbation from the zonal mean, * indicates the residual circulation, v is meridional wind, w is vertical wind and θ is potential temperature. The Eliassen-Palm flux divergence is given by

$$\nabla \cdot \overline{F} = \frac{1}{a\cos\phi}\frac{d}{d\phi}[f_\phi \cos\phi] + \frac{dF_z}{dz}, \quad \text{where} \tag{6}$$

$$F_\phi = \rho_0 a\cos\phi\left[\frac{\overline{v'\theta'}\,d\bar{u}/dz}{d\bar{\theta}/dz} - \overline{v'u'}\right] \quad \text{and} \tag{7}$$

$$F_z = \rho_0 a\cos\phi\left\{\left[f - \frac{1}{a\cos\phi}\frac{d(\bar{u}\cos\phi)}{d\phi}\right]\frac{\overline{v'\theta'}}{d\bar{\theta}/dz} - \overline{w'u'}\right\} \tag{8}$$

Figs. 15 and 16 show the first four terms in the zonal momentum equation (Eq. (4)) averaged over respectively the $Ls \sim 270°$ transfer event and following ('gap') period during spin-up year 12. In the absence of additional forces (such as damping and diffusion), the zonal-mean acceleration of an atmospheric region (the LHS of the equation, term1) should be equal to the sum of acceleration due to meridional (term2) and vertical (term3) transport by the residual mean circulation plus the acceleration due to non-angular-momentum conserving eddies (term4). Thus plot a in each figure should be equal to the sum of the other three, with plot d representing wave-driven angular momentum transport. In both Figs. 15 and 16, the strong Hadley circulation at this time of year, with overall rising motion in the south and flow from south to north aloft, is responsible for the pattern of plots b and c, which relate to respectively $-\bar{v}^*$ and $-\bar{w}^*$. Although the contours are saturated in plots b through d, the large degree of cancelation between the different angular momentum transport processes (residual mean meridional and vertical, and eddy driven) results in relatively small net increases or decreases in zonal wind (plot a). By comparing plots b–d with plot a, it is possible to attribute the acceleration of the mean flow to each transport process.

Fig. 15 shows the terms during the Ls 270° transfer event that occurred during the spin-up year shown in Fig. 12. By comparing plots a–d, we can identify the increase in equatorial zonal wind (term1, plot a) at ~1 mbar as being due to eddy-driven angular momentum transport (plot d). The EP flux divergence is positive in this region, denoting acceleration of the mean flow (see Eq. (4)), and negative at northern mid-to-high latitudes, denoting deceleration of the mean flow. This pressure level corresponds roughly to the base of the zonal jet peak at this point in this simulation (not shown).

By contrast, Fig. 16 shows the same terms during the 'gap period' (beginning at Ls 278°) that followed this transfer event. Now there is no significant equatorial acceleration of the zonal wind (plot a) and no significant eddy transport in this region (plot d). The low latitude acceleration produced just south of the equator at ~0.1 mbar by the residual mean vertical circulation (plot c) is more than canceled out by the residual mean meridional flow (plot b).

Figs. 17 and 18 show the EP flux vectors $\underline{F} = [F\phi, Fz]$ (Eqs. (7) and (8)) plotted over term4 (Eq. (4)) and focusing on the upper atmosphere region (which includes 1 mbar). Fig. 17 shows the EP fluxes for the same transfer event examined in Fig. 15, while Fig. 18 shows them for the same gap period as in Fig. 16. During the transfer event, the EP flux vectors appear horizontal and show propagation of wave activity from equatorial and low southern latitudes toward mid-to-high northern latitudes. This, along with the direction of momentum transport (i.e., toward the equator), suggests that the waves transport westward angular momentum from the equator toward the northern hemisphere, thus accelerating the equatorial region and decelerating higher northern latitudes (e.g., Schneider and Liu, 2009). By contrast, the EP fluxes are much smaller during the following gap period, implying little wave-driven angular momentum transport.

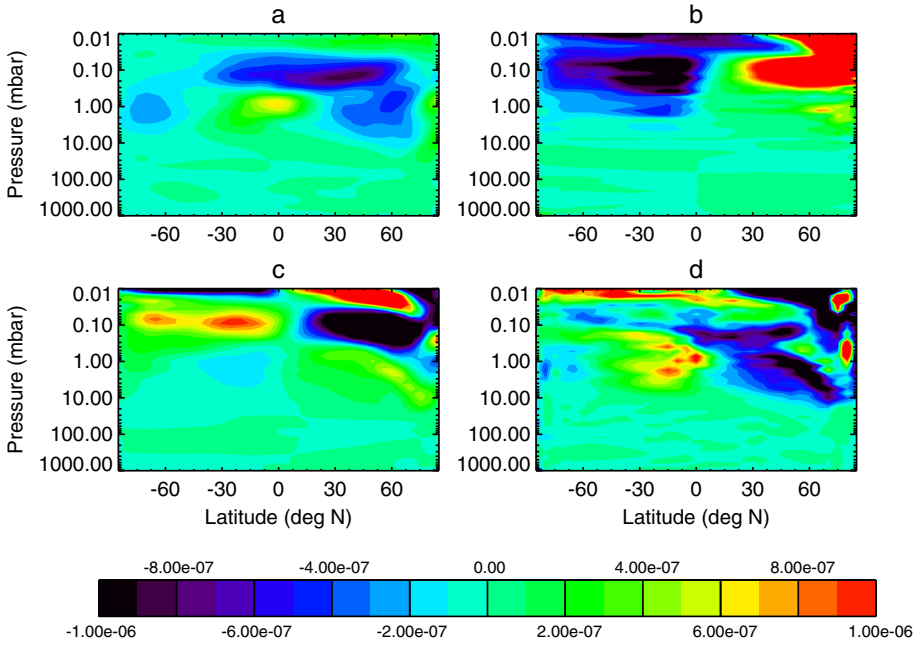

Fig. 15. Terms in the TEM zonal momentum equation (Eq. (4)) in ms^{-2} averaged over 12 days during the $Ls \sim 270°$, spin-up year 12 transfer event shown in Figs. 11 and 12. See text for details. (a) term1; (b) term2; (c) term3; (d) term4.

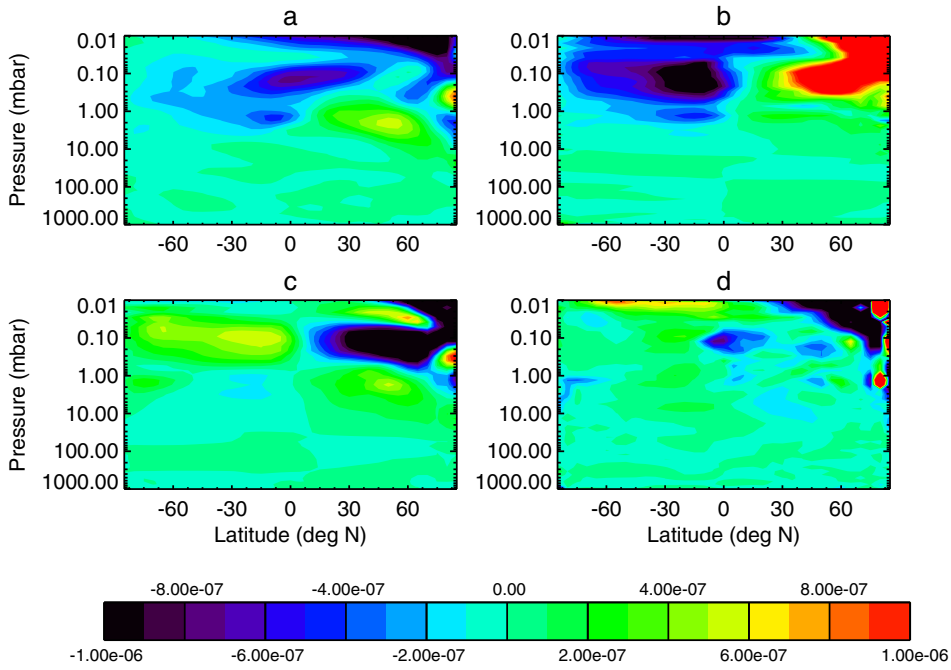

Fig. 16. As Fig. 15, but averaged over 12 Titan days in the 'gap period' (beginning at $Ls \sim 278°$) following the $Ls \sim 270°$ transfer event shown in Figs. 11 and 12.

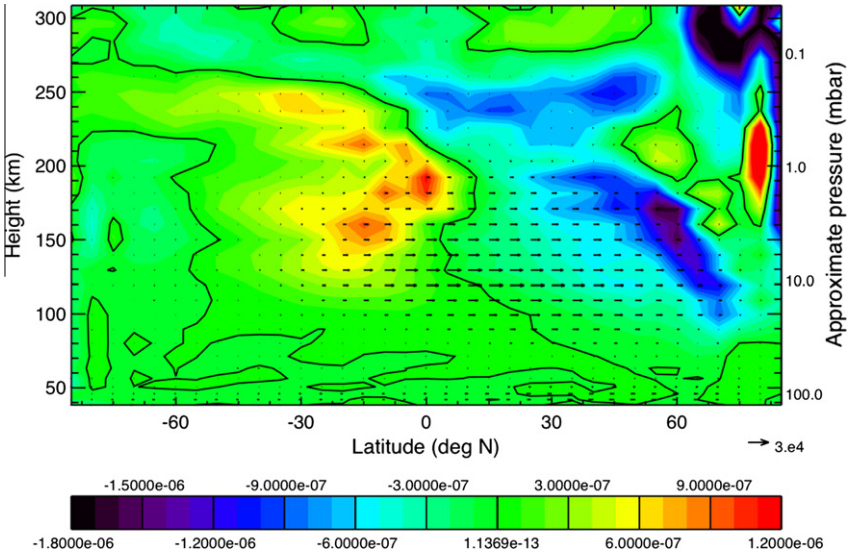

Fig. 17. EP flux divergence term (term4 in Eq. (4) in ms^{-2}, shown as contours) and EP flux vectors (in kg s^{-2}, shown in arrows) during spin-up year 12, averaged over 12 Titan days during the $Ls \sim 270°$ transfer event shown in Fig. 15. Note that the pressure axis shows the correct pressure range, but is only approximate as it assumes a fixed logarithmic relationship between pressure and height over this region.

4.3. Critical layers and wave breaking

The next step is to understand why the eddies produced in the TitanWRF v2 atmosphere have the above-described impact on the mean flow. According to linear theory, eddies are expected to break and deposit angular momentum into the mean flow in 'critical layers,' which exist where the eddies' zonal phase speed is close to the background zonal wind speed (e.g., Yamamoto and Takahashi, 2004, 2006; Mitchell and Vallis, 2010). Fig. 19 shows the eddy momentum flux cospectra as a function of phase speed and latitude for the 0.8 mbar pressure level during the $Ls \sim 270°$ transfer events and subsequent gap periods in spin-up year 12 and steady state year 75. For year 12 these periods were longer, and 12 days of data were used, whereas in year 75 only 6 days were used in each case; in all cases, variables were output 48 times per day. As in e.g. Randel and Held (1991), we first ran a Fourier analysis on the eddy momentum flux ($u'v'$) and calculated each wave's phase speed (which is a function of latitude and frequency). Then using bins 1/100th the size of the peak zonal mean wind speed we found the total amplitude in each phase speed bin (i.e., summing over all waves with phase speeds in that range, and over all wavenumbers present). Also shown in each plot is the zonal-mean zonal wind for the same pressure level and time period. The wave amplitudes are clearly far weaker during the gap periods (plots b and d) than during the transfer events (plots a and c), with faster and stronger waves present during the steady state transfer event (plot c) than during spin-up (plot a).

During both transfer events shown in Fig. 19, the strong eddy momentum flux is convergent at the equator ($u'v' < 0$ in the

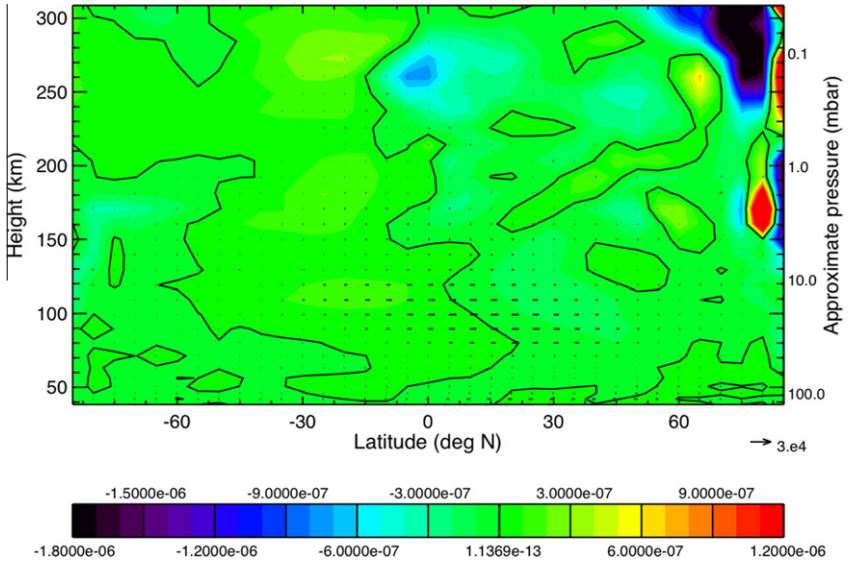

Fig. 18. As Fig. 17, but for the $Ls \sim 278°$ 'gap period' shown in Fig. 16.

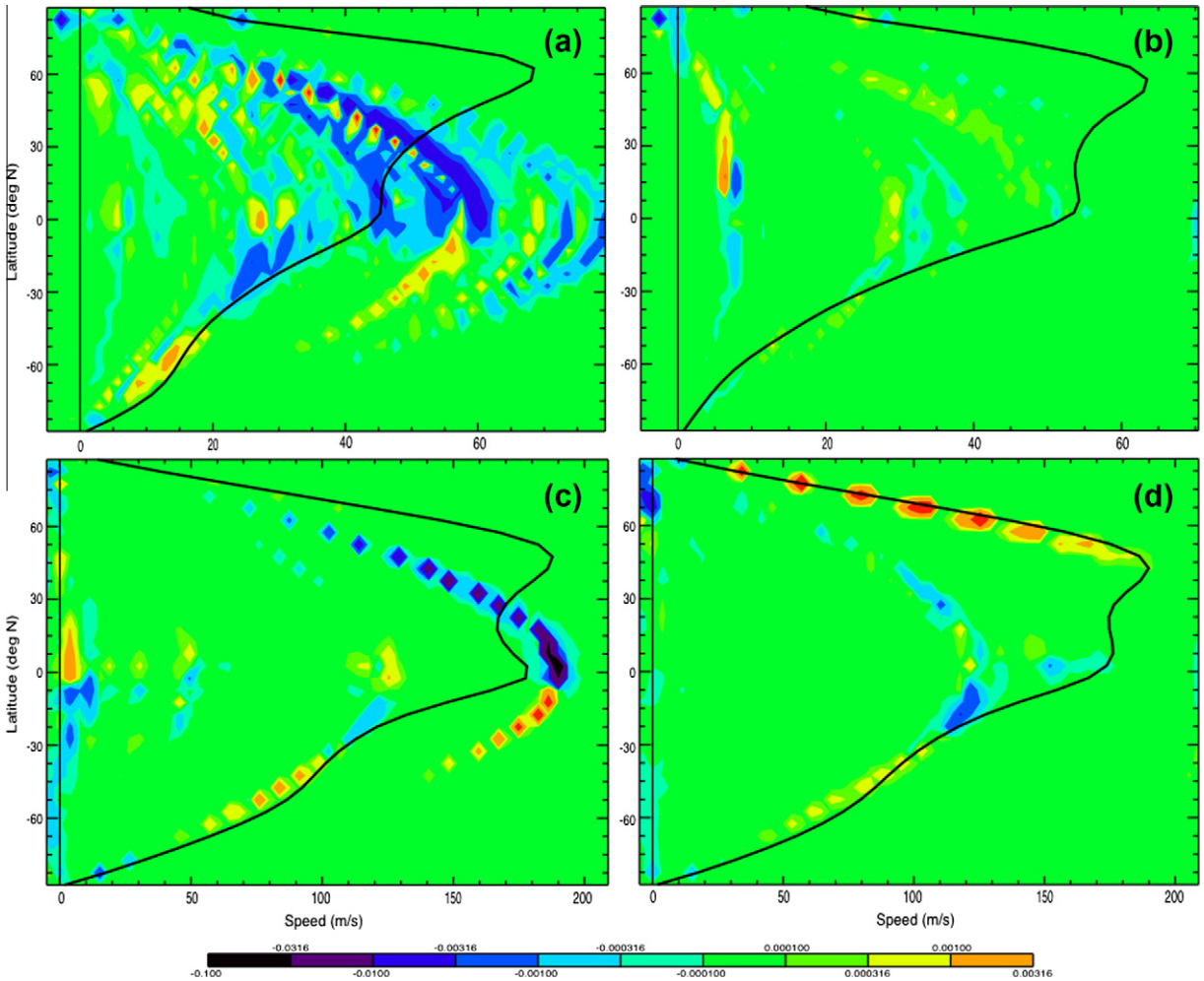

Fig. 19. Phase speed-latitude plot of eddy momentum flux cospectra (in $m^2\ s^{-2}$, shown as contours) and zonal-mean zonal wind (in ms^{-1}, thick black line) at 0.8 mbar, averaged over all zonal wavenumber for four different times. Top left: spin-up year 12, $Ls \sim 270°$ transfer event. Top right: spin-up year 12, $Ls \sim 278°$ 'gap' period. Bottom left: steady state year 75, $Ls \sim 270°$ transfer event. Bottom right: steady state year 75, $Ls \sim 278°$ 'gap' period.

northern hemisphere, and far weaker but positive in the southern hemisphere) and the waves are moving faster than the background flow, thus they deposit eastward momentum and accelerate the mean flow at low latitudes. These waves then appear to cross the critical layer (given by the zonal-mean zonal wind line) at ~25°–30°N and remain coherent up to ~50°–60°N. Once they have

crossed the critical layer the waves are traveling westward with respect to the mean flow, so now deposit westward angular momentum into the mean flow, decelerating it at these higher latitudes. This is entirely consistent with the transfers of eastward (positive) angular momentum from the northern to the equatorial region at this time of year, as shown in Figs. 12–14.

4.4. The nature of the eddies

In the above sections we focused on the impact of eddies on the mean flow. We now look at the eddies themselves, focusing on those most important for generating or maintaining superrotation during the transfer event periods shown in Fig. 19. A Fourier analysis of the perturbation zonal wind, meridional wind and temperature fields output 48 times per day shows large westward-propagating diurnal and semi-diurnal tides, which are expected to decrease rather than increase the superrotation of the equatorial region. The analysis also reveals several large-amplitude eastward-propagating waves, dominated by wavenumber 1, with some wavenumber 2 but very few wavenumber 3 (or higher) modes with any significant spectral power.

During the spin-up period transfer event, when the background zonal wind peaked at $\sim$70 ms^{-1}, the frequencies of the largest wavenumber 1 waves ranged from $\sim$5 to $\sim$7.5 per Titan day (relative to a fixed longitude on the surface). We identified the wave with phase speeds closest to the critical layer at the most latitudes as having a frequency of 5.1 per Titan day. Similarly, for the steady state transfer event, when the background zonal wind peaked at almost 190 ms^{-1}, the largest wave (which also had a phase speed close to the critical layer at many latitudes) had a frequency of 16.3 per day. The higher frequency (hence phase speed) of the dominant waves in the spun-up model is clearly linked to the faster superrotation of the atmosphere by this time. These waves are also completely absent in the following gap periods (not shown), thus are strong candidates for increasing superrotation during the transfer event.

Figs. 20 and 21 show the u, v and T amplitudes of the wavenumber 1, 5.1 per Titan day and wavenumber 1, 16.3 per Titan day waves during the spin-up and steady state transfer events, respectively. Noticeable in all plots is the concentration of peak amplitudes around the $\sim$1 mbar level, with the waves mostly confined between $\sim$0.2 and 3 mbar. Also interesting is that, while peak wave amplitudes in u and T occur above the equator, peak amplitudes in v occur at $\sim$30°–40°N.

Figs. 22 and 23 show the same waves in the eddy momentum flux ($u'v'$), with peak amplitudes occurring between $\sim$0 and 50°N. Again, their 'pancaked' appearance, now trapped between $\sim$0.5 and 2 mbar in pressure, is to be expected for a strongly stratified atmosphere.

Aside from the structure and frequency of these global waves, another important question is how they are formed. Are they produced by barotropic instabilities, as suggested by e.g. Gierasch (1975) and Rossow and Williams (1979), or by some other mechanism? Whatever the mechanism, it seems clear that it generates waves which then affect the mean flow (as demonstrated by e.g. the change in the zonal-mean zonal wind following a transfer event, Fig. 19) so as to remove or mitigate the conditions responsible for producing the instability.

The condition for quasi-geostrophic barotropic instability (Kuo, 1949, 1973) is that

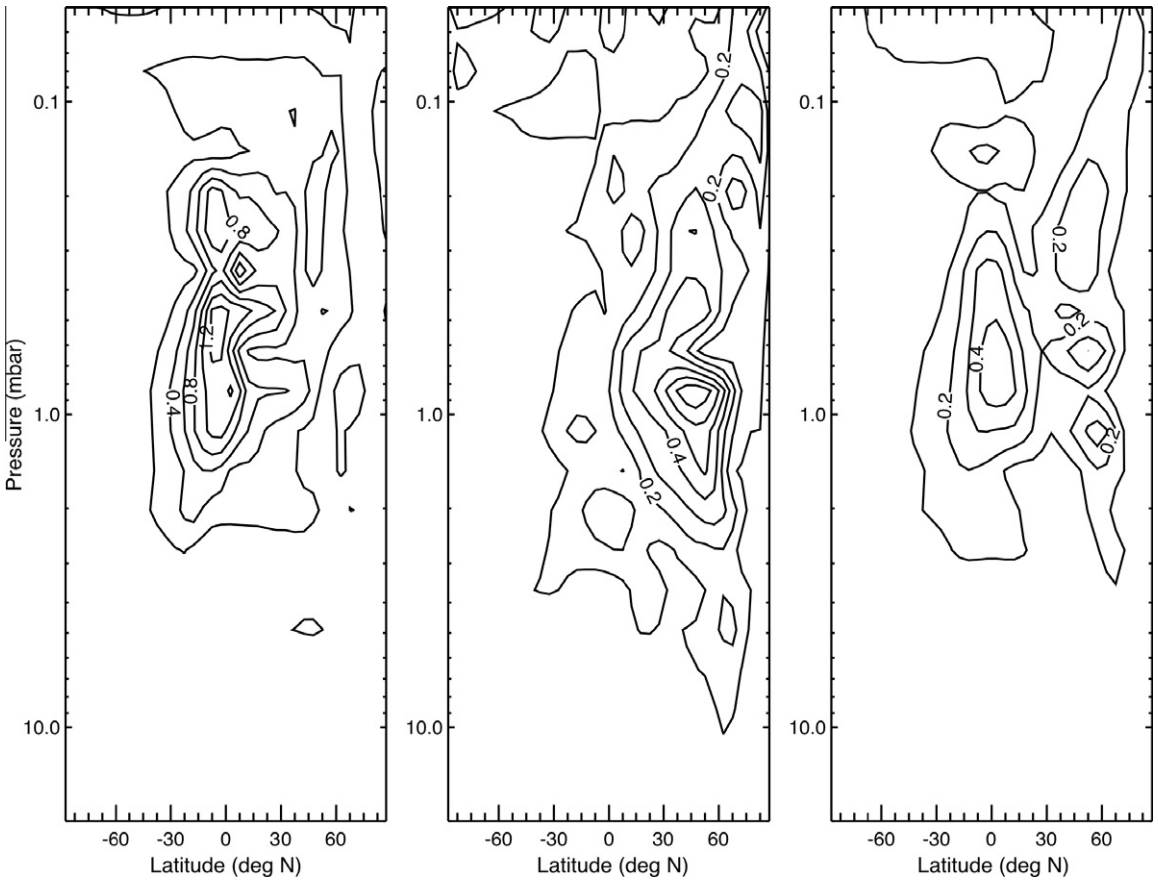

Fig. 20. Perturbation zonal wind (u', left), meridional wind (v', middle) and temperature (T', right) wave amplitudes for the largest eastward-propagating wave with phase speed close to the mean zonal wind speed during the $Ls \sim 270°$ transfer event in spin-up year 12. Wavenumber = 1, phase frequency = 5.08333 per day.

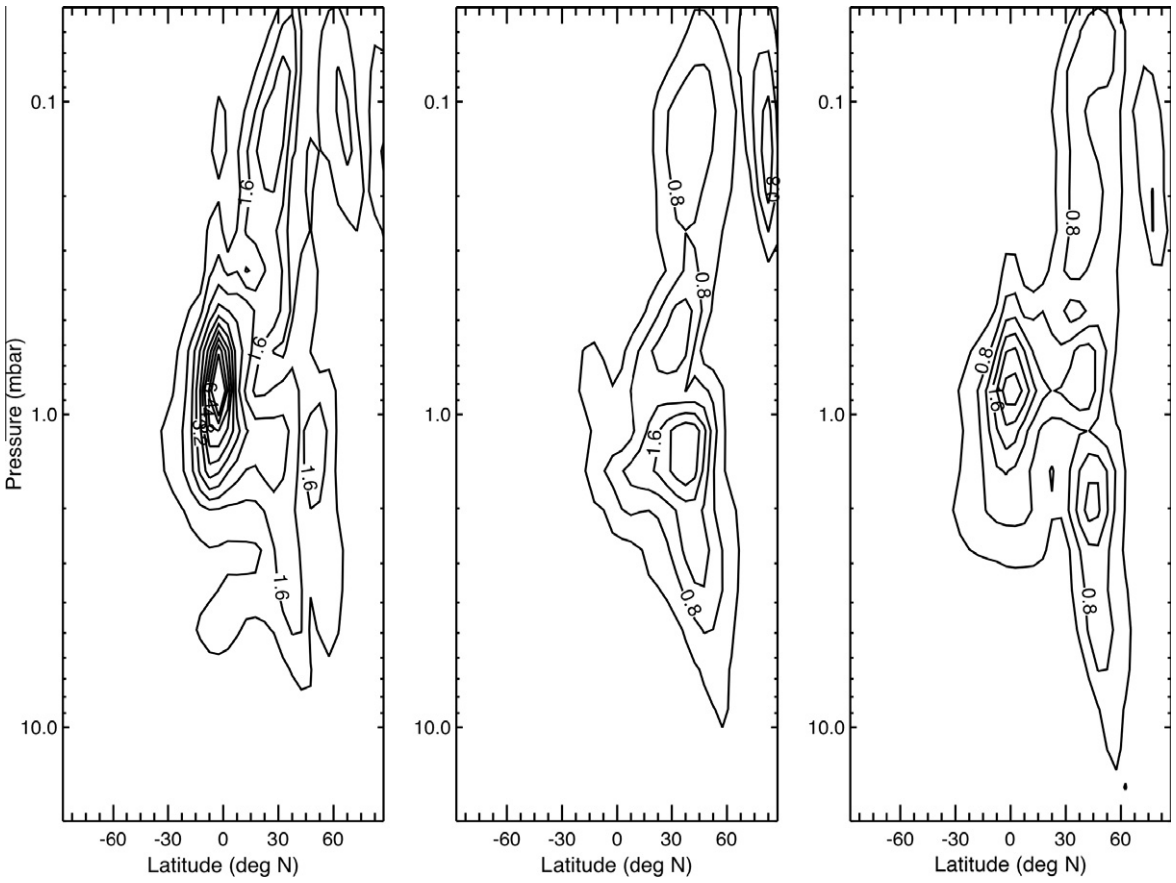

Fig. 21. As in Fig. 20 but for the $Ls \sim 270°$ transfer event in steady state year 75. Wavenumber = 1, phase frequency = 16.3 per day. Contour intervals are four times larger than in Fig. 20, reflecting the larger wave amplitudes in the spun-up model.

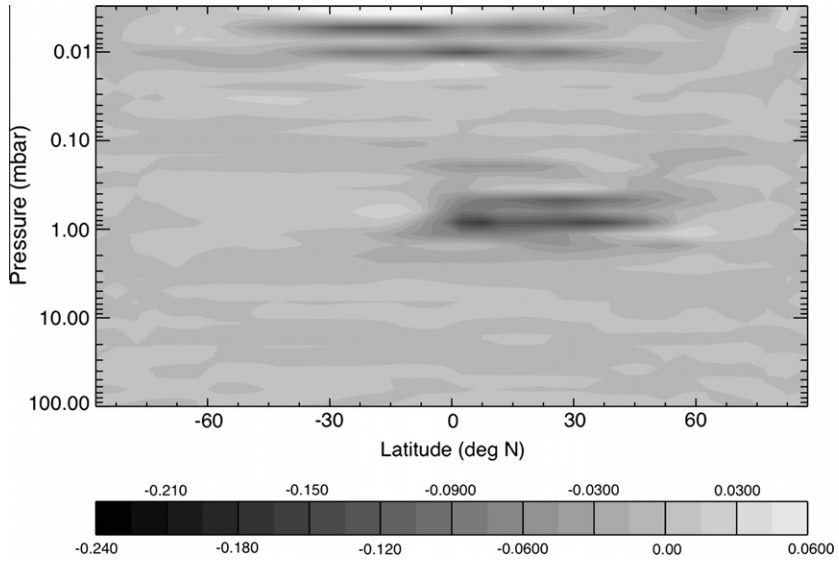

Fig. 22. Eddy momentum flux ($u'v'$) amplitude in $m^2\ s^{-2}$ of the year 12 (spin-up period) wave shown in Fig. 20.

$$\partial^2 \bar{u}/dy^2 - \beta = 0 \tag{9}$$

somewhere in the domain, where $\beta = df/dy = \frac{2\Omega \cos\phi}{a}$. This is unsatisfactory for Titan, as the moon's slow rotation rate means that the geostrophic approximation in not valid through most of the atmosphere, but it may provide some insight into how atmospheric instabilities build over time. We thus define a 'barotropic instability parameter,' ς, as the left hand side of Eq. (9), and plot this parameter in Fig. 24, averaged over the upper atmosphere region for spin-up

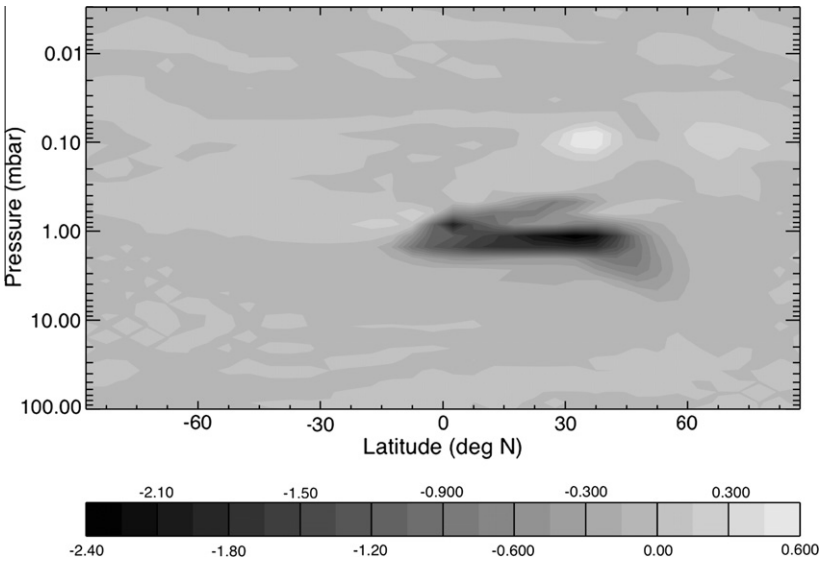

Fig. 23. As Fig. 22 but for the year 75 (steady state period) wave shown in Fig. 21.

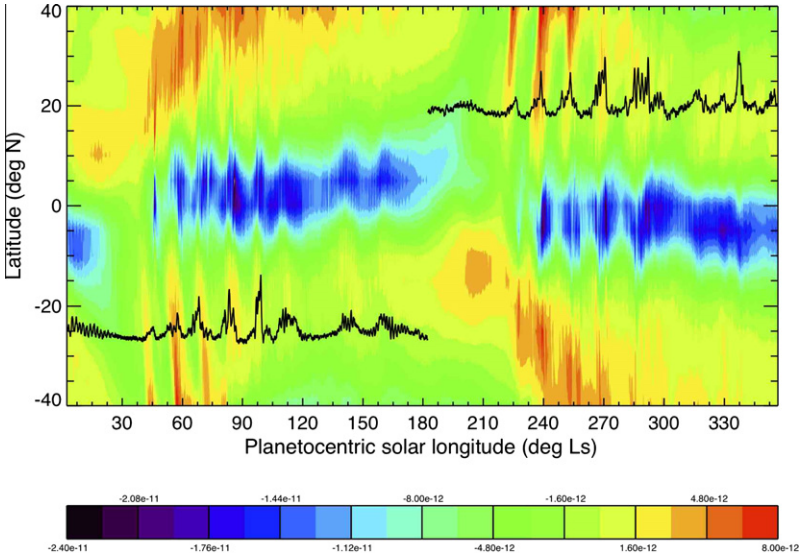

Fig. 24. Barotropic instability parameter, ς, averaged over the 24 model levels lying within the upper atmosphere region defined in Fig. 10 (in $m^{-1}\ s^{-1}$, shown in contours), and rate of change of angular momentum, dM/dt, in the equatorial upper atmosphere (solid black line), for spin-up year 12. Note that the y-axis positioning of dM/dt has been arbitrarily chosen to aid comparison with changes in ς.

year 12. Also shown for comparison of timings is dM/dt for the equatorial upper atmosphere in the same year (previously shown as the green line in the top plot of Fig. 9).

The QG barotropic instability criterion is met ($\varsigma = 0$) when the contours change from pale green to yellow-green. Although the significance is unclear, it is interesting to note that the transfer events (sharp increases in dM/dt) appear to occur immediately after such color changes occur, when 'fingers' of high ς extend into otherwise 'green' ($\varsigma < 0$) low-latitude regions, at ~0°–10°S from $Ls \sim 30°$ to 210°, and from ~0° to 10°N from $Ls \sim 210°$ to 30°. Further work is clearly required, however, to tie these waves definitively to a barotropic origin.

5. Discussion and further work

By removing any imposed sub-grid scale horizontal diffusion from the TitanWRF v2 general circulation model we are able to simulate realistically strong latitudinal temperature gradients, zonal wind jets and equatorial superrotation in TitanWRF's stratosphere. The model takes ~69 Titan years to spin-up from rest, i.e., reach a steady state in which the seasonal circulations approximately repeat from year to year. During spin-up, equatorial superrotation is generated by episodic angular momentum transfer events due to non-conservative waves which, as shown by e.g. EP flux diagnostics, transport westward angular momentum from low latitudes into the late fall through early spring hemisphere, accelerating the low latitudes and decelerating the fall/winter jet core. Once the model has reached steady state the transfer events are generally shorter in duration, suggesting that in its balanced state the atmosphere experiences shorter periods of instability.

Del Genio et al. (1993) performed simulations with a simplified Earth GCM run at Titan- and Venus-like rotation rates, and found a weakly dissipative environment to be vital for the production of superrotation, though focused on suppression of vertical mixing (below planetwide clouds) rather than on reduced horizontal mixing. Del Genio and Zhou (1996) found the reduction of numerical

dissipation to be vital to producing superrotation in a Venus-like model, though not for Titan (where results were more robust). However, as in Mitchell and Vallis (2010), all these experiments were performed with the seasonal cycle removed, i.e., with solar forcing that did not vary with time. This is significant, as we find huge differences between the spin-up of TitanWRF with time-invariant versus seasonally-varying forcing. Using time-invariant forcing similar to that of Del Genio et al. or Mitchell and Vallis, we find that superrotation (peaking high above the equator) builds rapidly, reaching over a hundred m/s in just a few Titan years, and that this occurs even if significant horizontal diffusion is present. It therefore seems that the mechanisms generating the initial superrotation are quite different between these constant forcing models and the more realistic TitanWRF simulations presented here, in which similar mechanisms appear to be at work during the spin-up and steady state periods.

The mechanisms maintaining superrotation once all models have reached steady state appear to have more similarities, with barotropic instabilities and the generation and propagation of low wavenumber waves appearing to play key roles in both constant forcing models (e.g., Del Genio and Zhou, 1996; Mitchell and Vallis, 2010) and in models with seasonal forcing (Hourdin et al., 1995; this paper). However, the model final states look quite different: for example, constant forcing models do not have seasons, so never produce jets that are asymmetric about the equator (as shown in Fig. 8). Identifying similarities between the mechanisms thus requires more investigation, and will be dealt with in a follow-up paper.

Looking in more detail at the eddies and processes involved in superrotation for TitanWRF, analysis of selected transfer events reveals the dominant waves at these times of year to be eastward propagating, zonal wavenumber 1 waves, with frequencies of ~5–7.5 per Titan day and ~16.3 waves per Titan day, respectively. These waves have convergent eddy momentum fluxes at low latitudes, and thus accelerate the mean flow there before propagating polewards through a critical layer in which the mean flow exceeds the phase speed of the waves. Linear theory predicts that at this point the waves should begin to break, depositing westward momentum and decelerating the mean flow in the jet core. To date we have analyzed only a small fraction of our total dataset (which includes dozens of transfer events per year, and tens of spin-up and steady state years), and we will explore this dataset more rigorously in the near future. However, our preliminary analysis suggests that the relevant eddies responsible for superrotation always form at low latitudes between ~10 and 0.01 mbar, propagate across the equator into the early fall through early spring hemisphere, decelerate the zonal flow there and accelerate the zonal flow in their source region, and thus spin-up (or maintain superrotation of) the equatorial stratosphere.

The transfer events appear to follow (or at least coincide with) low-latitude increases in barotropic instability, thus there is some suggestion that the waves responsible for generating and maintaining superrotation are generated by this mechanism. However, our analysis is not yet conclusive, and identifying the mechanism responsible for producing the waves, and hence superrotation, is the primary goal of future work and will be detailed in a follow-up paper. Other outstanding questions include: How do the dominant wavenumbers and frequencies change as the model evolves during spin-up toward steady state? At steady state, what waves are responsible for equatorward momentum transport at different seasons? How consistent are the dominant wavenumbers and frequencies from year to year?

A major question here, as with all model-based results, is whether the features and mechanisms identified in TitanWRF are those that actually occur on Titan itself. Given the initial difficulties experienced by ourselves, and by several other modeling groups, we are naturally keen to demonstrate that our solution to the superrotation problem – and our findings regarding the mechanisms at work – are robust, rather than limited to one extant numerical model. For this reason we are developing a second Titan GCM, based on the highly-efficient cubed-sphere MITgcm (Adcroft et al., 2004), and will repeat our experiments using this model in the near future.

An obvious validation approach is to compare our predicted wave types with those observed; however, the rather sparse nature of Cassini-based observations makes it difficult to look for short-lived episodic events in the data, particularly as a comparison of steady state years 75 and 76 suggests that, aside from their broad seasonal dependence, the precise timing of transfer events varies significantly from year to year, so we cannot predict exactly what to look for at a given *Ls*. In addition, CIRS data can only be used to produce temperature maps separated by ~Earth weeks, where 1 Earth week is roughly half a Titan day. This would thus allow the identification of waves with longer periods, but effectively rules out the precise identification of waves with periods that are much shorter than a Titan day, as we predict will dominate.

Remaining problems with our modeled atmosphere include the mismatch between the observed and modeled height (and to a lesser extent magnitude) of the zonal jet peak, which is ~60 km too low and ~10 m/s too weak in TitanWRF compared with Cassini CIRS data. These issues may be related to the relatively low model top, which may be impeding the upper atmosphere circulation hence affecting adiabatic heating in the winter hemisphere and thus temperature gradients and winds. They may also be due to the lack of active haze transport, which precludes feedbacks between haze microphysics, the circulation (via advection of haze particles) and radiative transfer. Rannou et al. (2004) showed that such coupling of haze microphysics and dynamics in their 2D model was able to reinforce their meridional circulation, increasing the strength of superrotation and better reproducing observations. This suggests that a similar result may be produced in a 3D GCM, in which additional feedbacks will be present between haze and eddies. Future work will therefore include the upwards extension of the model domain and the inclusion of haze microphysics and advection.

Acknowledgments

We thank Christopher McKay for providing us with his updated Titan radiative transfer scheme. We thank the WRF model development teams at NCAR, particularly Jimy Dudhia, Joseph Klemp, John Michalakes and William Skamarock, for their vital participation and assistance in extending WRF to run as a global model. We also thank Cassini CIRS team members Peter Gierasch, Richard Achterberg, Barney Conrath and Michael Flasar, for providing us with CIRS retrievals of temperature and inferred zonal wind, and for valuable discussions. We also thank our two anonymous reviewers for their very helpful and detailed comments. This work was funded by grants from NASA's Outer Planets Research program and the NASA Astrobiology Institute, and simulations were performed on the CITerra cluster in the GPS division at Caltech and on the Pleiades cluster at the High End Computing facility at NASA Ames.

References

Achterberg, R.K., Conrath, B.J., Gierasch, P.J., Flasar, F.M., Nixon, C.A., 2008a. Titan's middle-atmospheric temperatures and dynamics observed by the Cassini Composite Infrared Spectrometer. Icarus 194, 263–277. doi:10.1016/j.icarus.2007.09.029.

Achterberg, R.K., Conrath, B.J., Gierasch, P.J., Flasar, F.M., Nixon, C.A., 2008b. Observation of a tilt of Titan's middle-atmospheric superrotation. Icarus 197, 549–555. doi:10.1016/j.icarus.2008.05.014.

Achterberg, R.K., Gierasch, P.J., Conrath, B.J., Flasar, F.M., Nixon, C.A., 2011. Temporal variations of Titan's middle-atmospheric temperatures from 2004 to 2009 observed by the Cassini/CIRS. Icarus 211, 686–698. doi:10.1016/j.icarus.2010.08.009.

Adcroft, A., Campin, J.-M., Hill, C., Marshall, J., 2004. Implementation of an atmosphere–ocean general circulation model on the expanded spherical cube. Mon. Weather Rev. 132 (12), 2845–2863.

Andrews, D.G., McIntyre, M.E., 1978. Generalized Eliassen-Palm and Charney-Drazin theorems for waves on axisymmetric mean flows in compressible atmospheres. J. Atmos. Sci. 35, 175–218.

Andrews, D.G., Holton, J.R., Leovy, C.B., 1987. Middle Atmosphere Dynamics. Academic Press, Orlando, FL.

Del Genio, A.D., Zhou, W., Eichler, T.P., 1993. Equatorial superrotation in a slowly rotating GCM: Implications for Titan and Venus. Icarus 101, 1–17. doi:10.1006/icar.1993.1001.

Del Genio, A.D., Zhou, W., 1996. Simulations of superrotation of slowly rotating planets: Sensitivity to rotation and initial condition. Icarus 120, 332–343. doi:10.1006/icar.1996.0054.

Flasar, F.M., Samuelson, R.E., Conrath, B.J., 1981. Titan's atmosphere: Temperature and dynamics. Nature 292 (5825), 693–698.

Flasar, F.M. et al., 2005. Titan's atmospheric temperatures, winds, and composition. Science 308 (5724), 975–978.

Folkner, W.M. et al., 2006. Winds on Titan from ground-based tracking of the Huygens probe. J. Geophys. Res. 111, E07S02. doi:10.1029/2005JE002649.

Friedson, A.J., West, R.A., Wilson, E.H., Oyafuso, F., Orton, G.S., 2009. A global climate model of Titan's atmosphere and surface. Planet. Space Sci. 57 (14–15), 1931–1949.

Gierasch, P.J., 1975. Meridional circulation and the maintenance of the Venus atmospheric rotation. J. Atmos. Sci. 32, 1038–1044.

Hide, R., 1969. Dynamics of the atmospheres of the major planets with an appendix on the viscous boundary layer at the rigid bounding surface of an electrically-conducting rotating fluid in the presence of a magnetic field. J. Atmos. Sci. 26, 841–853.

Hong, S.-Y., Pan, H.-L., 1996. Nonlocal boundary layer vertical diffusion in a medium-range forecast model. Mon. Weather. Rev. 124, 2322–2339.

Hourdin, F., Talagrand, O., Sadourny, R., Courtin, R., Gautier, D., McKay, C.P., 1995. Numerical simulation of the general circulation of the atmosphere of Titan. Icarus 117, 358–374.

Hubbard, W.B. et al., 1993. The occultation of 28 Sgr by Titan. Astron. Astrophys. 269, 541–563.

Kostiuk, T., Fast, K.E., Livengood, T.A., Hewagama, T., Goldstein, J.J., Espenak, F., Buhl, D., 2001. Direct measurement of winds on Titan. Geophys. Res. Lett. 28 (12), 2361–2364. doi:10.1029/2000GL012617.

Kuo, H.-L., 1949. Dynamic instability of two-dimensional nondivergent flow in a barotropic atmosphere. J. Meteorit. 6 (2), 105–122.

Kuo, H.-L., 1973. Dynamics of quasigeostrophic flows and instability theory. Adv. Appl. Mech. 13, 247–300.

Luz, D., Hourdin, F., Rannou, P., Lebonnois, S., 2003. Latitudinal transport by barotropic waves in Titan's stratosphere. II. Results from a coupled dynamics–microphysics–photochemistry GCM. Icarus 166, 343–358.

McKay, C.P., Pollack, J.B., Courtin, R., 1989. The thermal structure of Titan's atmosphere. Icarus 80, 23–53.

Mingalev, I.V., Mingalev, V.S., Mingalev, O.V., Kazeminejad, B., Lammer, H., Biernat, H.K., Lichtenegger, H.I.M., Schwingenschuh, K., Rucker, H.O., 2006. First simulation results of Titan's atmosphere dynamics with a global 3-D non-hydrostatic circulation model. Ann. Geophys. 24, 2115–2129.

Mitchell, J.L., 2008. The drying of Titan's dunes: Titan's methane hydrology and its impact on atmospheric circulation. J. Geophys. Res. (Planets) 113, E12. doi:10.1029/2007JE003017.

Mitchell, J.L., Vallis, G.K., 2010. The transition to superrotation in terrestrial atmospheres. J. Geophys. Res. 115, E12008. doi:10.1029/2010JE003587.

Mitchell, J.L., Pierrehumbert, R.T., Frierson, D.M.W., Caballero, R., 2006. The dynamics behind Titan's methane clouds. Proc. Natl. Acad. Sci. USA 103 (49), 18421–18426.

Newman, C.E., Richardson, M.I., Lee, C., Toigo, A.D., Ewald, S.P., 2008. The TitanWRF model at the end of the Cassini Prime Mission. Am. Geophys. Union, Fall Meeting. Abstract #P12A-02.

Ponte, R.M., Rosen, R.D., 1993. Determining torques over the ocean and their role in the planetary momentum budget. J. Geophys. Res. 98 (D4), 7317–7325. doi:10.1029/92JD02953.

Radebaugh, J. et al., 2008. Dunes on Titan observed by Cassini Radar. Icarus 194 (2), 690–703.

Randel, W.J., Held, I.M., 1991. Phase speed spectra of transient eddy fluxes and critical layer absorption. J. Atmos. Sci. 48, 688–697.

Rannou, P., Hourdin, F., McKay, C.P., Luz, D., 2004. A coupled dynamics–microphysics model of Titan's atmosphere. Icarus 170, 443–462.

Richardson, M.I., Toigo, A.D., Newman, C.E., 2007. PlanetWRF: A general purpose, local to global numerical model for planetary atmospheric and climate dynamics. J. Geophys. Res. (Planets) 112, E09001. doi:10.1029/2006JE002825.

Rossow, W.B., Williams, G.P., 1979. Large-scale motion in the Venus stratosphere. J. Atmos. Sci. 36 (3), 377–389.

Schneider, E.K., 1977. Axially symmetric steady-state models of the basic state for instability and climate studies. Part II. Nonlinear calculations. J. Atmos. Sci. 34, 280–296.

Schneider, T., Liu, J., 2009. Formation of jets and equatorial superrotation on Jupiter. J. Atmos. Sci. 66 (3), 579–601. doi:10.1175/2008JAS2798.1.

Strobel, D.F., 2006. Gravitational tidal waves in Titan's upper atmosphere. Icarus 182 (1), 251–258. doi:10.1016/j.icarus.2005.12.015.

Tokano, T., Neubauer, F.M., 2002. Tidal winds on Titan caused by Saturn. Icarus 158, 499–515.

Tokano, T., Neubauer, F.M., Laube, M., McKay, C.P., 1999. Seasonal variation of Titan's atmospheric structure simulated by a general circulation model. Planet. Space Sci. 47, 493–520.

Yamamoto, M., Takahashi, M., 2004. Dynamics of Venus' superrotation: The eddy momentum transport processes newly found in a GCM. Geophys. Res. Lett. 31, L09701. doi:10.1029/2004GL019518.

Yamamoto, M., Takahashi, M., 2006. Superrotation maintained by meridional circulation and waves in a Venus-like AGCM. J. Atmos. Sci. 63, 3296–3314.